UAV-Enabled Integrated Sensing and Communication in Maritime Emergency Networks

Bohan Li, *Member, IEEE*, Jiahao Liu, Junsheng Mu, Pei Xiao, *Senior Member, IEEE*, and Sheng Chen, *Life Fellow, IEEE*

***Abstract*—With the line-of-sight mode deployment and fast response, an uncrewed aerial vehicle (UAV), equipped with the cutting-edge integrated sensing and communication (ISAC) technique, is poised to deliver high-quality communication and sensing (CAS) services in maritime emergency scenarios. In practice, however, the real-time transmission of ISAC signals at the UAV side cannot be realized unless a reliable wireless fronthaul link between the terrestrial base station (TBS) and UAV is available. This article proposes a multicarrier-division duplex (MDD)-based joint fronthaul-access scheme, where mutually orthogonal subcarrier sets are leveraged to simultaneously support four types of fronthaul/access transmissions. In order to maximize the end-to-end communication rate while maintaining an adequate sensing quality-of-service (QoS) in such a complex scheme, the UAV trajectory, subcarrier assignment, and power allocation are jointly optimized. The overall optimization process is designed in two stages. As the emergency area is usually far away from the coast, the optimal initial operating position for the UAV is first found. Once the UAV passes the initial operating position, the UAV's trajectory and resource allocation are optimized during the mission period to maximize the end-to-end communication rate under the constraint of minimum sensing QoS. Simulation results demonstrate the effectiveness of the proposed scheme in dealing with the joint fronthaul-access optimization problem in maritime ISAC networks, offering the advantages over benchmark schemes.**

***Index Terms*—Integrated sensing and communication (ISAC), maritime emergency network (MEN), multicarrier-division duplex (MDD), uncrewed aerial vehicle (UAV).**

I. Introduction

MARITIME rescue is never an easy task. Apart from natural factors, the limited capability of maritime communication and sensing (CAS) is the main challenge rendering the maritime rescue extremely difficult [1]. Without sufficiently high-data-rate communications and accurate sensing, the fast and effective rescue carried out several kilometers away from the coast is infeasible. To this end, advanced maritime emergency networks (MENs) have been investigated. In particular, the Global Maritime Distress and Safety System (GMDSS) is the most widely used maritime rescue system at present, which is composed of terrestrial base stations (TBSs) and satellite networks, to provide long-range coverage of maritime communication and positioning services [2]. However, subject to the long distance from TBS and satellite to the emergency area, the GMDSS suffers from a restricted data rate, low-resolution sensing, and large latency, failing to meet the demand of wideband communication and accurate sensing on the ocean.

By contrast, due to high flexibility and easy deployment, uncrewed aerial vehicles (UAVs) are more competitive for constituting temporary emergency networks [3], and they can achieve a higher transmission rate and enhanced communication coverage in the target area [4]. As for sensing, satellites and TBSs are better at searching the widely unknown area, while UAVs are capable of quickly approaching the targets and implementing the high-resolution positioning and detection works once the location of the interested area is roughly known [5]. Despite these advantages, there is a paucity of works that leverage UAVs to simultaneously execute the emergency tasks of CAS on the ocean. This is mainly because, at present, concurrently employing both communication and radar equipment may impose a significant energy burden on the UAV, leading to a reduced mission period. However, it is not the case in the near future of beyond 5G and 6G eras, as the integrated sensing and communication (ISAC) technology will enable the UAV to simultaneously carry out CAS on a common hardware platform, thereby largely saving energy consumption [6].

A. Related Works

1) UAV-Aided MCNs: To date, there have been many works studying the UAV-aided maritime communication networks (MCNs) [7]. Lyu et al. [8], Qian et al. [9], and Xin et al. [10] proposed various UAV trajectory/deployment optimization and resource allocation algorithms to achieve different objectives in MCN, such as maximizing data collection capability of UAV [8], minimizing UAV's total energy consumption [9], and achieving the optimal system spectral efficiency [10]. However, the aforementioned works only consider the access link from the UAV to maritime users, but ignore the fronthaul link

Received 17 August 2025; accepted 5 October 2025. Date of publication 8 October 2025; date of current version 8 December 2025. This work was supported in part by the National Key Research and Development Program of China under Grant 2024YFC3109100, in part by the National Natural Science Foundation of China under Grant 62401530, and in part by the Natural Science Foundation of Shandong Province under Grant ZR2024QF076. *(Corresponding author: Jiahao Liu.)*

Bohan Li and Jiahao Liu are with the Faculty of Information Science and Engineering, the Engineering Research Center of Advanced Marine Physical Instruments and Equipment, Ministry of Education, and Qingdao Key Laboratory of Optics and Optoelectronics, Ocean University of China, Qingdao 266100, China (e-mail: bohan.li@ouc.edu.cn; ljh4327@ouc.edu.cn).

Junsheng Mu is with the School of Information and Communication Engineering, Beijing University of Posts and Telecommunications, Beijing 100876, China (e-mail: mu_junsheng@126.com).

Pei Xiao is with the 5G/6G Innovation Centre, University of Surrey, GU2 7XH Guildford, U.K. (e-mail: p.xiao@surrey.ac.uk).

Sheng Chen is with the School of Electronics and Computer Science, University of Southampton, SO17 1BJ Southampton, U.K. (e-mail: sqc@ecs.soton.ac.uk).

Digital Object Identifier 10.1109/JIOT.2025.3619130

from the TBS to the UAV. In fact, it is the fronthaul link that makes MCN different from terrestrial networks in the presence of UAV-aided communications. More specifically, in terrestrial networks, with the aid of a handover technique among cells or sufficient bandwidth, e.g., millimeter-waveband, the UAV can usually connect to a BS in its proximity or have plenty of spectral resources. Hence, the performance of the fronthaul link can be maintained [11]. By contrast, for MCN, once the UAV flies far away from the TBS, its trajectory design and resource allocation must carefully consider the fronthaul link, as the degradation of which will highly hinder the achievable access rate.

2) UAV-Enabled ISAC: Driven by its features of on-demand deployment and line-of-sight (LoS)-dominant channels, the UAV-enabled ISAC (UAV-ISAC) has garnered tremendous attention recently [6]. Liu et al. [12], Wang et al. [13], Meng et al. [14], Lyu et al. [15], Liu et al. [16], Deng et al. [17], and Khalili et al. [18] studied the optimization of UAV trajectory/deployment and resource allocation to maximize the communication data rate or minimize the energy consumption while attaining adequate quality of service (QoS) for sensing. The sensing-centered schemes have also been proposed in [19], [20], and [21], where the optimization aims to maximize the accuracy of localization or detection subject to adequate communication QoS. Instead of dealing with single-objective optimization, Rezaei et al. [22], Jing et al. [23], and Bayessa et al. [24] concurrently optimized CAS relying on a weighted sum formulation. Here, three critical issues are worth further discussing.

First, in UAV-ISAC-related papers, the metrics of sensing performance can be generally classified into two categories, i.e., information-theoretic metrics [12], [14], [15], [18], [20], [21], [22], [24], [25], such as sensing mutual information (MI), sensing SINR, and radar estimation rate, and estimation-theoretic metrics [13], [17], [19], [23], such as Cramér–Rao bound and mean square error. Information-theoretic metrics are independent of the estimator, which makes system optimization more general, while estimation-theoretic metrics are only used for explicitly characterizing the performance of a specific sensing task.

Second, in order to mitigate the interference between CAS functions, most of the papers applied the time-division method to transmit communication signal and receive sensing echo at different time slots [12], [14], [16], [17], [18], [19], [22], [25], while Zhang et al. [20] proposed the frequency-division method such that CAS signals can be transmitted over orthogonal bands. Both of these methods suppress the interference at the expense of time or frequency resources. In addition, Lyu et al. [15] implemented CAS using separate beams at the same time–frequency grid, but this approach inevitably causes residual digital-domain interference, especially when targets and users are located in similar directions.

Third, only [12], [13], [18], [20], [21], and [25], considered the fronthaul links in UAV-ISAC systems. In particular, [12], [20], [21], and [25] leveraged the fronthaul links to feed the sensed information back to the data center, among which [21] and [25] used the access links to implement ISAC services, while [12] and [20] only transmitted sensing signal over the access links. Moreover, Khalili et al. [18] took the performance of fronthaul links into account, over which the UAV exchanges both the sensing and communication data with the BS, while ISAC transmissions are conducted over access links. However, in the proposed scheme, the UAV sequentially implements single-target sensing, communication, and two types of fronthaul transmissions, which may result in lower efficiency when the number of potential targets significantly increases. Note that the above-mentioned papers adopted the decode-and-forward mode to implement the sensing task, which requires the UAV to first process the sensed information based on its own baseband processor, and then forward the decoded sensing data to the data center. In this case, the UAV may suffer from extra computational overhead, resulting in reduced flight time.

B. Motivations and Contributions

1) Motivations: Against the above background, in this article, we exploit the UAV-ISAC technique in MENs, which has not been well-studied in open literature to the best of our knowledge. To make the application of UAV-ISAC in maritime emergency scenarios a reality, there are three challenges to be properly solved.

1) To satisfy the requirements of high transmission rate and low end-to-end latency in MENs, the full-duplex (FD) design of the ISAC waveform is necessary. In this case, the interference between CAS within the same time slot and frequency band has to be carefully addressed.
2) Maritime emergency usually happens far away from the coast, and hence the performance of the long-range wireless fronthaul links between the UAV and TBS is essential. In other words, to ensure the high-quality real-time downlink (DL) communication and target sensing, the fronthaul and access links must be jointly optimized in MENs.
3) As the timely CAS services are of paramount importance in MENs, it would be too late to provide services upon UAV's arrival at the emergency spot. Instead, the feasible services should be offered as early as possible after the UAV takes off. Therefore, in order to achieve timely CAS in MENs, the UAV's trajectory has to be specifically designed. These challenges motivate us to design a tailor-made ISAC waveform and frame structure for MENs, and jointly consider the fronthaul and access links during the optimization of resource allocation and UAV's trajectory, so as to obtain the optimal system performance.

2) Contributions: The novelties and contributions of this article are summarized as follows.

1) We design a UAV-ISAC scheme for MENs. To mitigate the interference between DL CAS echo signals and improve the end-to-end performance, the multicarrier-division duplex (MDD)-based ISAC waveform is proposed, in which the TBS-to-UAV fronthaul link, UAV-to-TBS fronthaul link, UAV-to-user DL link, and UAV-to-target sensing link are assigned with four mutually orthogonal subcarrier sets. To compensate for the frequency loss caused by subcarrier-division

TABLE I
CONTRASTING OUR PROPOSED SCHEME WITH THE LITERATURE OF UAV-ISAC SCHEMES

	Proposed	[19]	[20]	[18, 25]	[6, 14, 16, 17, 22]	[13, 15, 23, 24]	[12, 21]
Maritime scenario	✓						
ISAC transmission	✓	✓	✓	✓	✓	✓	✓
End-to-end sensing MI	✓						
Frame structure design	✓	✓		✓	✓		
FD-like waveform	✓						
Joint fronthaul-access optimization	✓		✓	✓			✓
UAV's trajectory design	✓	✓	✓	✓	✓	✓	✓
Joint power-subcarrier allocation	✓	✓	✓				

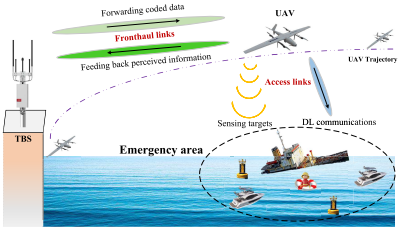

Fig. 1. UAV-ISAC-enabled MEN.

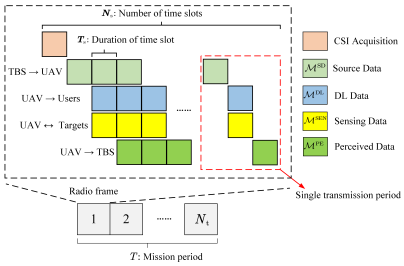

Fig. 2. Frame structure of UAV-enabled MEN operating on MDD mode.

operation, an advanced multistream frame structure is tailor-made for the proposed networks, due to the FD characteristic of MDD [26].

2) Considering the requirements of real-time CAS services in an emergency area, the fronthaul links between the UAV and the TBS are practically modeled. Two different operating modes, decode-and-forward and amplify-and-forward, are applied at the UAV side to process the coded DL data from the TBS and the perceived information to the TBS, respectively. The end-to-end sensing MI between targets and the TBS based on the amplify-and-forward mode is derived to evaluate the sensing performance, which has not been studied in the existing UAV-ISAC scenarios.
3) In order to maximize the end-to-end DL rate while maintaining adequate sensing QoS, two subproblems with respect to the optimization of UAV trajectory, power allocation at UAV and TBS sides, and subcarrier assignment within fronthaul and access links are presented. More specifically, considering the fact that the UAV cannot implement the CAS immediately after taking off due to the long distance away from the interested area, the first subproblem aims to find the UAV's optimal initial operating location. Then, the second subproblem maximizes the end-to-end DL rate under the constraint of minimum sensing MI during the mission period.

Finally, a brief comparison between our proposed scheme with the existing UAV-ISAC works is shown in Table I.

II. SYSTEM MODEL

Consider a UAV-assisted MEN which includes a TBS, a fixed-wing UAV, U mobile users (ships requiring communication service) constituting the set $\mathcal{U}$, and J maritime targets (buoys, ships, and other surface vehicles) constituting the set $\mathcal{J}$, as shown in Fig. 1. The on-demand UAV is deployed near the coast. Once the emergency occurs, the UAV flies toward the designated area to constitute an airborne network. Equipped with the ISAC technique, the UAV concurrently communicates with mobile users and senses targets at the same time and frequency band. The TBS is based along the coast and acts as the CPU establishing wireless fronthaul links with the UAV for forwarding the source data to and receiving the perceived information from the UAV. To meet the stringent energy limit of UAVs and avoid the overhead of extra radio frequency (RF) components at the UAV, the fronthaul and access links share the spectrum.

Both the TBS and UAV operate in MDD mode. Specifically, all the subcarriers, defined by the index set $\{m|m \in \mathcal{M}, |\mathcal{M}| = M\}$ within the frequency band, are coarsely classified into two blocks, i.e., $\mathcal{M}^D$ and $\mathcal{M}^S$, for implementing DL- and sensing-related tasks, respectively. Assumed that CAS are of equal importance in the proposed maritime emergency scenario, the first $M/2$ subcarriers within $\mathcal{M}$ constitute $\mathcal{M}^D$, while the last $M/2$ subcarriers constitute $\mathcal{M}^S$. At the nth radio frame, $\mathcal{M}^D$ is further divided into $\mathcal{M}_n^{\mathrm{SD}}$ and $\mathcal{M}_n^{\mathrm{DL}}$, which are used to transmit source data at the TBS and implement DL communications at the UAV, respectively. Similarly, $\mathcal{M}^S$ is further cut into $\mathcal{M}_n^{\mathrm{SEN}}$ and $\mathcal{M}_n^{\mathrm{PE}}$ for the UAV to carry out sensing and feedback the perceived signal to the TBS, respectively. Note that the way of fine division of $\mathcal{M}^D$ and $\mathcal{M}^S$ is flexible and time-variant, dependent on the specific scenario. Denoted by $\alpha_{n,m}^X \in \{0,1\}$, $X \in \{\mathrm{DL}, \mathrm{SEN}, \mathrm{PE}, \mathrm{SD}\}$, the indicator of subcarrier assignment at the nth radio frame. If $\alpha_{n,m}^X = 1$, then $m \in \mathcal{M}_n^X$. According to the principle of MDD, we have

$$\alpha_{n,m}^{\mathrm{DL}} + \alpha_{n,m}^{\mathrm{SEN}} + \alpha_{n,m}^{\mathrm{PE}} + \alpha_{n,m}^{\mathrm{SD}} \le 1 \quad \forall n, m \in \mathcal{M}. \tag{1}$$

The frame structure is illustrated in Fig. 2, where the mission period T consists of N_t radio frames, and each radio frame includes N_s time slots. It is assumed that during each radio frame, the UAV and mobile users are quasistationary and stay at fixed locations, while the channel state information (CSI) of fronthaul and access channels remains unchanged.

Hence, the transmission procedure during a single transmission period can be described as follows.

1) The UAV receives the pilots from users and derives the CSI of DL channels.[1]
2) The UAV sends pilots and DL CSI to the TBS, who then estimates the CSI of the channel from the UAV to itself. Since the UAV and TBS leverage two orthogonal subcarrier sets within the same frequency band for two-way fronthaul transmissions, the two-way fronthaul channels exhibit time-domain reciprocity and frequency-domain correlation. Consequently, the TBS can derive the CSI of the channel from itself to the UAV.
3) The TBS sends source data to the UAV based on the users' request, and feeds back the CSI of the fronthaul channel to the UAV. In addition, as the TBS may have access to the rough image of the emergency area via satellite remote sensing, it can provide the UAV with approximate coordinates of the interested area so that the UAV can implement quick sensing. Note that the delivery of CSI and auxiliary sensing coordinates can be achieved via control channels and, therefore, will not affect system optimization.
4) The UAV adopts the decode-and-forward relay mode, which enables the UAV to first decode the data received from the TBS, and then forward it to users. Depending on the a priori information of targets' locations, the UAV leverages DL data to carry out sensing tasks.[2]
5) The UAV resorts to the amplify-and-forward relay mode, by which the UAV is able to first amplify the echo signals, and then transmit the perceived information to the TBS for final sensing decision.

A. CAS Links

The UAV is equipped with $R_{\text{tx}} = R_{\text{tx}}^{l} \times R_{\text{tx}}^{w}$ transmit and $R_{\text{rx}} = R_{\text{rx}}^{l} \times R_{\text{rx}}^{w}$ receive uniform planar arrays (UPAs), which are placed parallel to the ground and sea surface. As shown in Fig. 2, at the tth time slot of the nth radio frame, the integrated fronthaul, CAS signal transmitted by the UAV over the mth subcarrier, can be expressed as (2), as shown at the bottom of the page, where $\boldsymbol{w}_{\text{SEN}}^{j}[n,m]$ ($x_{\text{SEN}}^{j}[n,t,m]$), $\boldsymbol{w}_{\text{DL}}^{u}[n,m]$ ($x_{\text{DL}}^{u}[n,t,m]$), and $\boldsymbol{w}_{\text{PE}}^{j}[n,m]$ ($x_{\text{PE}}^{j}[n,t,m]$) denote the precoders (data) for sensing target j, communicating with user u, and sending the perceived information of target j back to the TBS, respectively, with each data having unit energy, i.e., $\mathbb{E}[|x[n,t,m]|^2] = 1$. The transmit power of the UAV is constrained by $\sum_{m=1}^{M} \mathbb{E}[\|\boldsymbol{s}[n,t,m]\|^2] \le P_{\text{UAV}}$.

Remark 1: Since the UAV receives the source data and sensing echo while transmitting the integrated signal, it suffers from self-interference (SI). We assume that the UAV can rely on the combination of passive cancellation methods (e.g., implementing antenna separation between transmit and receive arrays [27], and placing an RF absorber among transceiver [28]) and active cancellation methods (e.g., multitap RF canceller [29] and adaptive beamforming-aided suppression [30]) to provide sufficient analog-domain SI cancellation (SIC) such that the power of SI falls into the dynamic range of ADC. Then, due to the characteristic of MDD [26], the reception of the source signal is free from the digital-domain SI with the aid of the fast Fourier transform (FFT) operation. As for the reception of echo signal, although the digital interference components of DL and perceived signal can be readily removed by FFT, the transmitted sensing signal directly arriving at the receiver gives rise to the digital-domain SI, which can be modeled as $\boldsymbol{z}_{\text{SI}}[n,m] \in \mathbb{C}^{R_{\text{rx}}} \sim \mathcal{CN}\left(\boldsymbol{0}, \alpha_{n,m}^{\text{SEN}} \xi_{\text{SIC}} \sum_{j=1}^{J} \|\boldsymbol{w}_{\text{SEN}}^{j}[n,m]\|^2 \boldsymbol{I}_{R_{\text{rx}}}\right)$, where ξ_{SIC} denotes the SIC capability at the UAV taking account the analog- and digital-domain SI suppression.

At the UAV, the received echo signal reflected from target j at the mth subcarrier is given in (3), as shown at the bottom of the next page, where $\boldsymbol{x}_{\text{SEN}}[n,t,m] = [x_{\text{SEN}}^{1}[n,t,m], \ldots, x_{\text{SEN}}^{J}[n,t,m]]^{\text{T}}$, $\boldsymbol{\Lambda}_{\text{SEN}}[n,m] = \text{diag}(\boldsymbol{W}_{\text{SEN}}[n,m]) \in \mathbb{C}^{R_{\text{tx}}J \times J}$ with $\boldsymbol{W}_{\text{SEN}}[n,m] = [\boldsymbol{w}_{\text{SEN}}^{1}[n,m], \ldots, \boldsymbol{w}_{\text{SEN}}^{J}[n,m]] \in \mathbb{C}^{R_{\text{tx}} \times J}$, $\text{diag}(\cdot)$ denoting the block diagonal transformation, $\widetilde{\boldsymbol{W}}_{\text{SEN}}[n,m] = [\widetilde{\boldsymbol{w}}_{\text{SEN}}^{1}[n,m], \ldots, \widetilde{\boldsymbol{w}}_{\text{SEN}}^{J}[n,m]] \in \mathbb{C}^{R_{\text{rx}} \times J}$ with $\widetilde{\boldsymbol{w}}_{\text{SEN}}^{j}[n,m] \in \mathbb{C}^{R_{\text{rx}}}$ denoting the echo combining vector for target j, and $\boldsymbol{H}_{\text{SEN}}[n,m] = [(\boldsymbol{H}_{\text{SEN}}^{1}[n,m])^H, \ldots, (\boldsymbol{H}_{\text{SEN}}^{J}[n,m])^H]^H \in \mathbb{C}^{R_{\text{tx}}J \times R_{\text{rx}}}$ is the concentrated sensing channels of targets with $\boldsymbol{H}_{\text{SEN}}^{j}[n,m] \in \mathbb{C}^{R_{\text{tx}} \times R_{\text{rx}}}$ given in (4), while $\boldsymbol{n}_{\text{UAV}}[n,m] \sim \mathcal{CN}(\boldsymbol{0}, N_0 \boldsymbol{I}_{R_{\text{rx}}})$ denotes the additive white Gaussian noise with N_0 representing noise power spectrum density. As we assume that targets are sparsely distributed, the terms of interbeam interference caused by transmit antenna sidelobes, i.e., $\{\widetilde{\boldsymbol{w}}_{\text{SEN}}^{j}[n,m](\boldsymbol{H}_{\text{SEN}}^{a}[n,m])^H \boldsymbol{w}_{\text{SEN}}^{b}[n,m] x_{\text{SEN}}^{b}[n,t,m] | \forall a,b \in$

[1] As we mainly study the MDD-aided optimization tradeoff among fronthaul and access links in maritime ISAC scenarios, the perfect CSI is assumed as in [14], [21], and [25], to avoid the deviation of the core of this article.

[2] Although the targets' locations are known at the current time slot, they may be changed at the next time slot. Hence, the sensing tasks aim at detecting whether the targets are still located at the same positions, or tracking the targets' new positions based on the previous ones.

$$\boldsymbol{s}[n,t,m] = \begin{cases} \boldsymbol{0}, & 1 \le t \le 2 \\ \alpha_{n,m}^{\text{SEN}} \sum_{j=1}^{J} \boldsymbol{w}_{\text{SEN}}^{j}[n,m] x_{\text{SEN}}^{j}[n,t,m] + \alpha_{n,m}^{\text{DL}} \sum_{u=1}^{U} \boldsymbol{w}_{\text{DL}}^{u}[n,m] x_{\text{DL}}^{u}[n,t,m], & t = 3 \\ \alpha_{n,m}^{\text{SEN}} \sum_{j=1}^{J} \boldsymbol{w}_{\text{SEN}}^{j}[n,m] x_{\text{SEN}}^{j}[n,t,m] + \alpha_{n,m}^{\text{DL}} \sum_{u=1}^{U} \boldsymbol{w}_{\text{DL}}^{u}[n,m] x_{\text{DL}}^{u}[n,t,m] & \\ \quad + \alpha_{n,m}^{\text{PE}} \sum_{j=1}^{J} \boldsymbol{w}_{\text{PE}}^{j}[n,m] x_{\text{PE}}^{j}[n,t,m], & t \ge 4 \end{cases} \tag{2}$$

$\mathcal{J}$ and $a \neq b\}$, are omitted to facilitate analysis. Unlike the complex scattering environment around TBS, the channels between the UAV and maritime users and targets are dominated by an LoS link. Therefore, the sensing channel $\boldsymbol{H}_{\mathrm{SEN}}^{j}[n,m]$ is given by

$$\begin{aligned}\boldsymbol{H}_{\mathrm{SEN}}^{j}[n,m] &= \sqrt{\frac{G_{\mathrm{UAV}}^{\mathrm{tx}} G_{\mathrm{UAV}}^{\mathrm{rx}} \lambda_m^2 \sigma_j^{\mathrm{RCS}}}{(4\pi)^3 d_j^4[n]}}\varpi_{j,n,m} e^{-\mathrm{j}2\pi\tau_j f_m} e^{\mathrm{j}2\pi f_{D,j} t_0} \\ &\quad \times \boldsymbol{\alpha}_{\mathrm{tx}}\left(\theta_j^{\mathrm{tx}}[n], \phi_j^{\mathrm{tx}}[n], m\right) \boldsymbol{\alpha}_{\mathrm{rx}}^{H}\left(\theta_j^{\mathrm{rx}}[n], \phi_j^{\mathrm{rx}}[n], m\right) \end{aligned} \tag{4}$$

where $G_{\mathrm{UAV}}^{\mathrm{tx}}$, $G_{\mathrm{UAV}}^{\mathrm{rx}}$, λ_m, σ_j^{RCS}, τ_j, t_0, $\varpi_{j,n,m} \sim \mathcal{CN}(0,1)$, f_m, and $f_{D,j}$ are the UAV transmitter and receiver antenna gains, wavelength, radar cross section (RCS), path delay, symbol duration, complex gain, center frequency of the mth subband, and Doppler frequency, respectively. The Doppler and delay effects are assumed to be perfectly compensated through synchronization [14]. The distance between the UAV and target j is given by $d_j[n] = \left\|\boldsymbol{c}_{\mathrm{UAV}}[n] - \boldsymbol{c}_j\right\|$, where $\boldsymbol{c}_{\mathrm{UAV}}[n] = [x_{\mathrm{UAV}}[n], y_{\mathrm{UAV}}[n], z_{\mathrm{UAV}}]$ and $\boldsymbol{c}_j = [x_j, y_j, z_j]$ denote the coordinates of the UAV and the jth target at the nth radio frame, respectively. The fly height of the UAV is assumed to be constant. Moreover, $\boldsymbol{\alpha}_{\mathrm{tx}}(\cdot)$ and $\boldsymbol{\alpha}_{\mathrm{rx}}(\cdot)$ denote the UPA response vectors of the UAV transmitter and receiver, respectively.

During the tth time slot of the nth radio frame, the DL communication signal of subcarrier m received at user u is given in (5) as shown at the bottom of the page, where $n_u[n,m] \sim \mathcal{CN}(0, N_0)$ and the DL communication channel is modeled as

$$\begin{aligned}\boldsymbol{h}_{\mathrm{DL}}^{u}[n,m] = &\sqrt{\frac{G_{\mathrm{UAV}}^{\mathrm{tx}} G_{\mathrm{UE}}^{\mathrm{rx}} \lambda_m^2}{(4\pi)^2 d_u^2[n]}}\varpi_{u,n,m} e^{-\mathrm{j}2\pi\tau_u f_m} e^{\mathrm{j}2\pi f_{D,u} t_0} \\ &\times \boldsymbol{\alpha}_{\mathrm{tx}}\left(\theta_u^{\mathrm{tx}}[n], \phi_u^{\mathrm{tx}}[n], m\right) \in \mathbb{C}^{R_{\mathrm{tx}}} \end{aligned} \tag{6}$$

in which $\varpi_{u,n,m} \sim \mathcal{CN}(0,1)$ and $d_u[n] = \|\boldsymbol{c}_{\mathrm{UAV}}[n] - \boldsymbol{c}_u\|_2$ with $\boldsymbol{c}_u = [x_u, y_u, z_u]$ denoting the coordinate of user u. As the subcarriers used for transmitting the source, sensing, and perceived signals are orthogonal to those used for DL transmissions, users only suffer from the cosubchannel multiuser interference.

B. Two-Way Fronthaul Links

The TBS sends the source data to the UAV using $\bar{R}_{\mathrm{tx}} = \bar{R}_{\mathrm{tx}}^{l} \times \bar{R}_{\mathrm{tx}}^{w}$ transmit UPA. The UAV works as the decode-and-forward relay to first decode the received data and then carry out CAS tasks. Due to the complex sensing environment and limited computation resources, the UAV adopts the amplify-and-forward method in the sensing task, that is, it only amplifies the received target echo and directly forward it to the TBS for sensing data processing. To distinguish the perceived information of different targets, the TBS equips with $\bar{R}_{\mathrm{rx}} = \bar{R}_{\mathrm{rx}}^{l} \times \bar{R}_{\mathrm{rx}}^{w}$ receive UPA.

The received source data at the UAV on subcarrier m is given by (7), as shown at the bottom of the next page, where $\widetilde{\boldsymbol{W}}_{\mathrm{SD}}[n,m] = [\widetilde{\boldsymbol{w}}_{\mathrm{SD}}^{1}[n,m], \ldots, \widetilde{\boldsymbol{w}}_{\mathrm{SD}}^{U}[n,m]] \in \mathbb{C}^{R_{\mathrm{rx}} \times U}$ is the UAV combiner for receiving the source data $\boldsymbol{x}_{\mathrm{SD}}[n,t,m] \in \mathbb{C}^{U}$ from the TBS. Under the TBS power constraint, the precoding matrix $\boldsymbol{F}_{\mathrm{SD}}[n,m] = [\boldsymbol{f}_{\mathrm{SD}}^{1}[n,m], \ldots, \boldsymbol{f}_{\mathrm{SD}}^{U}[n,m]] \in \mathbb{C}^{\bar{R}_{\mathrm{tx}} \times U}$ satisfies $\sum_{m \in \mathcal{M}} \alpha_{n,m}^{\mathrm{SD}} \|\boldsymbol{F}_{\mathrm{SD}}[n,m]\|_F^2 \leq P_{\mathrm{TBS}}$. Due to the strong LoS path and possible scatters around the TBS, the mth subchannel between the TBS and UAV during the nth radio frame follows the Rician distibution, which can be expressed as (8), as shown at the bottom of the next page, where $d_{\mathrm{TU}}[n] = \|\boldsymbol{c}_{\mathrm{TBS}} - \boldsymbol{c}_{\mathrm{UAV}}[n]\|_2$, $\boldsymbol{c}_{\mathrm{TBS}} = [x_{\mathrm{TBS}}, y_{\mathrm{TBS}}, z_{\mathrm{TBS}}]$ is the coordinate of TBS, K_{TU} is the Rician factor, and each entry of the small-fading matrix $\boldsymbol{\Psi}_{\mathrm{SD}}[n,m]$ follows the distribution $\mathcal{CN}(0,1)$.

As shown in Fig. 2, starting from $t = 4$, the TBS concurrently sends the source data to the UAV and receives the perceived data from the UAV relying on two orthogonal subcarrier sets within the same frequency band, and hence experiences analog-domain SI. Similar to the signal processing at the UAV, we also assume that the TBS is able to provide sufficient analog-domain SIC such that the power of residual analog-domain SI falls into the ADC dynamic range. Then, the residual digital-domain SI can be efficiently canceled by FFT. Consequently, at the TBS receiver, the signal of the mth subcarrier during the tth time slot of the nth radio frame is given in (9), as shown at the bottom of the next page, where $\widetilde{\boldsymbol{F}}_{\mathrm{PE}}[n,m] = [\widetilde{\boldsymbol{f}}_{\mathrm{PE}}^{1}[n,m], \ldots, \widetilde{\boldsymbol{f}}_{\mathrm{PE}}^{J}[n,m]] \in \mathbb{C}^{\bar{R}_{\mathrm{rx}} \times J}$ is the combining matrix for receiving the perceived signal of targets, $\boldsymbol{W}_{\mathrm{PE}}[n,m] = [\boldsymbol{w}_{\mathrm{PE}}^{1}[n,m], \ldots, \boldsymbol{w}_{\mathrm{PE}}^{J}[n,m]] \in \mathbb{C}^{R_{\mathrm{tx}} \times J}$, $\boldsymbol{n}_{\mathrm{TBS}}[n,m] \sim \mathcal{CN}(0, N_0 \boldsymbol{I}_{\bar{R}_{\mathrm{rx}}})$, and $\boldsymbol{H}_{\mathrm{PE}}[n,m] \in \mathbb{C}^{R_{\mathrm{tx}} \times \bar{R}_{\mathrm{rx}}}$ has a

$$\begin{aligned}\boldsymbol{r}_{\mathrm{PE}}[n,t,m] &= \left[x_{\mathrm{PE}}^{1}[n,t,m], \ldots, x_{\mathrm{PE}}^{J}[n,t,m]\right]^{\mathrm{T}} \\ &= \begin{cases} \boldsymbol{0}, & 1 \leq t \leq 2 \\ \alpha_{n,m}^{\mathrm{SEN}} \widetilde{\boldsymbol{W}}_{\mathrm{SEN}}^{H}[n,m] \boldsymbol{H}_{\mathrm{SEN}}^{H}[n,m] \boldsymbol{\Lambda}_{\mathrm{SEN}}[n,m] \boldsymbol{x}_{\mathrm{SEN}}[n,t,m] & \\ \quad + \widetilde{\boldsymbol{W}}_{\mathrm{SEN}}^{H}[n,m] \left(\boldsymbol{n}_{\mathrm{UAV}}[n,m] + \boldsymbol{z}_{\mathrm{SI}}[n,m]\right), & t \geq 3 \end{cases} \end{aligned} \tag{3}$$

$$y_u[n,t,m] = \begin{cases} 0, & 1 \leq t \leq 2 \\ \alpha_{n,m}^{\mathrm{DL}} \left(\boldsymbol{h}_{\mathrm{DL}}^{u}[n,m]\right)^{H} \boldsymbol{w}_{\mathrm{DL}}^{u}[n,m] x_{\mathrm{DL}}^{u}[n,t,m] & \\ \quad + \alpha_{n,m}^{\mathrm{DL}} \sum\limits_{u'=1, u' \neq u}^{U} \left(\boldsymbol{h}_{\mathrm{DL}}^{u}[n,m]\right)^{H} \boldsymbol{w}_{\mathrm{DL}}^{u'}[n,m] x_{\mathrm{DL}}^{u'}[n,t,m] + n_u[n,m], & t \geq 3 \end{cases} \tag{5}$$

similar form as $\boldsymbol{H}_{\mathrm{SD}}[n,m]$ in (8). As the subcarrier used for sensing is orthogonal to that for transmitting the perceived signal, the subcarrier m' in $\boldsymbol{r}_{\mathrm{PE}}[n,t,m']$ is different from the subcarrier m in other terms. Furthermore, we assume $|\mathcal{M}_n^{\mathrm{SEN}}| = |\mathcal{M}_n^{\mathrm{PE}}| = M/4$ and there are $M/4$ subcarrier pairs, i.e., $\mathcal{M}_n^{\mathrm{pair}} = \{(m,m')|m \in \mathcal{M}_n^{\mathrm{PE}}, m' \in \mathcal{M}_n^{\mathrm{SEN}}\}$, to sense and forward target information, where any subcarrier in $\mathcal{M}_n^{\mathrm{PE}}$ and $\mathcal{M}_n^{\mathrm{SEN}}$ can only be paired for once.

III. Optimization Problem Design

By employing the MDD, the subcarriers used for DL communication, sensing, and two-way fronthaul transmissions are mutually orthogonal, and the design of their corresponding digital beamforming vectors becomes independent. In order to focus on the joint optimization of UAV trajectory and MDD-enabled resource allocation to maximize the end-to-end communication rate of the proposed network while ensuring the sensing requirements, we adopt the conventional but highly efficient beamforming strategies to reduce the complexity of system optimization.

For two-way fronthaul links, due to the existence of non-negligible non-LoS channels, the ranks of $\boldsymbol{H}_{\mathrm{SD}}[n,m]$ and $\boldsymbol{H}_{\mathrm{PE}}[n,m]$ are much larger than the numbers of users and targets, respectively. Performing the singular value decomposition on $\boldsymbol{H}_{\mathrm{SD}}[n,m]$ and $\boldsymbol{H}_{\mathrm{PE}}[n,m]$ yields the effective channel matrices $\bar{\boldsymbol{H}}_{\mathrm{SD}}[n,m] = \boldsymbol{U}_{\mathrm{SD}}[n,m]\boldsymbol{\Lambda}_{\mathrm{SD}}^{1/2}[n,m]\boldsymbol{L}_{\mathrm{SD}}^{H}[n,m]$ and $\bar{\boldsymbol{H}}_{\mathrm{PE}}[n,m] = \boldsymbol{U}_{\mathrm{PE}}[n,m]\boldsymbol{\Lambda}_{\mathrm{PE}}^{1/2}[n,m]\boldsymbol{L}_{\mathrm{PE}}^{H}[n,m]$, where $\boldsymbol{U}_{\mathrm{SD}}[n,m] \in \mathbb{C}^{\bar{R}_{\mathrm{tx}}\times U}$ ($\boldsymbol{U}_{\mathrm{PE}}[n,m] \in \mathbb{C}^{R_{\mathrm{tx}}\times J}$) and $\boldsymbol{L}_{\mathrm{SD}}[n,m] \in \mathbb{C}^{R_{\mathrm{rx}}\times U}$ ($\boldsymbol{L}_{\mathrm{PE}}[n,m] \in \mathbb{C}^{\bar{R}_{\mathrm{rx}}\times U}$) are the reduced unitary submatrices corresponding to the singular matrices of $\boldsymbol{\Lambda}_{\mathrm{SD}}[n,m] = d_{\mathrm{TU}}^{-2}[n]\mathrm{diag}(\eta_{\mathrm{SD}}^1[n,m],\ldots,\eta_{\mathrm{SD}}^U[n,m])$ ($\boldsymbol{\Lambda}_{\mathrm{PE}}[n,m] = d_{\mathrm{TU}}^{-2}[n]\mathrm{diag}(\eta_{\mathrm{PE}}^1[n,m],\ldots,\eta_{\mathrm{PE}}^J[n,m])$). In order to avoid inter-stream interference and maximize the capacity of fronthaul links, we set $\boldsymbol{F}_{\mathrm{SD}}[n,m] = \boldsymbol{U}_{\mathrm{SD}}[n,m]\boldsymbol{\Sigma}_{\mathrm{SD}}^{1/2}[n,m]$, $\widetilde{\boldsymbol{W}}_{\mathrm{SD}}[n,m] = \boldsymbol{L}_{\mathrm{SD}}[n,m]$, $\boldsymbol{W}_{\mathrm{PE}}[n,m] = \boldsymbol{U}_{\mathrm{PE}}[n,m]\boldsymbol{\Sigma}_{\mathrm{PE}}^{1/2}[n,m]$, $\widetilde{\boldsymbol{F}}_{\mathrm{PE}}[n,m] = \boldsymbol{L}_{\mathrm{PE}}[n,m]$, where $\boldsymbol{\Sigma}_{\mathrm{SD}}[n,m] = \mathrm{diag}(p_{\mathrm{SD}}^1[n,m],\ldots,p_{\mathrm{SD}}^U[n,m])$, and $\boldsymbol{\Sigma}_{\mathrm{PE}}[n,m] = \mathrm{diag}(p_{\mathrm{PE}}^1[n,m],\ldots,p_{\mathrm{PE}}^J[n,m])$ denote the matrices of power allocation for source data and perceived sensing data transmissions, respectively.

Remark 2: Due to the existence of a strong LoS path between the TBS and UAV, for each subcarrier channel m used for transmitting perceived information, there is one singular value much larger than the others in $\boldsymbol{\Sigma}_{\mathrm{PE}}[n,m]$. In this case, considering the effective detection of all the targets, the largest singular value with respect to $|\mathcal{M}_n^{\mathrm{PE}}|$ subcarrier channels is equally distributed to J targets. In other words, the largest singular value is not always placed at the first diagonal position of $\boldsymbol{\Sigma}_{\mathrm{PE}}[n,m]$. Instead, the probability of its occurrence at every diagonal position is the same. By contrast, as the UAV adopts the decode-and-forward to pass through the DL signal from TBS to users, we mainly concern the total channel capacity of each subcarrier channel $\boldsymbol{H}_{\mathrm{SD}}[n,m]$, and therefore, the position of the largest singular value inside $\boldsymbol{\Sigma}_{\mathrm{SD}}[n,m]$ is inconsequential.

To strike a balance between low-complexity and satisfactory performance, we adopt matched-filtering precoding for communication and sensing links. The communication precoding matrix is derived as $\boldsymbol{W}_{\mathrm{DL}}[n,m] = [\boldsymbol{w}_{\mathrm{DL}}^1[n,m],\ldots,\boldsymbol{w}_{\mathrm{DL}}^U[n,m]] = [\boldsymbol{\alpha}_{\mathrm{tx}}(\theta_1^{\mathrm{tx}}[n],\phi_1^{\mathrm{tx}}[n],m),\ldots,\boldsymbol{\alpha}_{\mathrm{tx}}(\theta_U^{\mathrm{tx}}[n],\phi_U^{\mathrm{tx}}[n],m)]\boldsymbol{\Sigma}_{\mathrm{DL}}^{1/2}$, where $\boldsymbol{\Sigma}_{\mathrm{DL}} = \mathrm{diag}(p_{\mathrm{DL}}^1[n,m],\ldots,p_{\mathrm{DL}}^U[n,m])$ is the DL transmission power allocation matrix. The sensing transmit and receive beamformers are implemented as $\boldsymbol{W}_{\mathrm{SEN}}[n,m] = [\boldsymbol{\alpha}_{\mathrm{tx}}(\theta_1^{\mathrm{tx}}[n],\phi_1^{\mathrm{tx}}[n],m),\ldots,\boldsymbol{\alpha}_{\mathrm{tx}}(\theta_J^{\mathrm{tx}}[n],\phi_J^{\mathrm{tx}}[n],m)\boldsymbol{\Sigma}_{\mathrm{SEN}}^{1/2}$ and $\widetilde{\boldsymbol{W}}_{\mathrm{SEN}}[n,m] = [\boldsymbol{\alpha}_{\mathrm{rx}}(\theta_1^{\mathrm{rx}}[n],\phi_1^{\mathrm{rx}}[n],m),\ldots,\boldsymbol{\alpha}_{\mathrm{rx}}(\theta_J^{\mathrm{rx}}[n],\phi_J^{\mathrm{rx}}[n],m)]$, where $\boldsymbol{\Sigma}_{\mathrm{SEN}}[n,m] = \mathrm{diag}(p_{\mathrm{SEN}}^1[n,m],\ldots,p_{\mathrm{SEN}}^J[n,m])$ is the power allocation matrix for target sensing.

Intuitively, the end-to-end rate is related to the performance of both fronthaul and access transmissions. Denote by $R_{\mathrm{SD}}[n]$ and $R_{\mathrm{DL}}[n]$, the nth radio frame achievable rate of the TBS sending source data to the UAV and the nth radio frame achievable rate of the UAV transmitting DL data to users, respectively. Based on (5) and (7), $R_{\mathrm{SD}}[n]$ and $R_{\mathrm{DL}}[n]$ can be expressed as follows:

$$R_{\mathrm{SD}}[n] = \frac{N_s-1}{N_s} \times \sum_{m\in\mathcal{M}} \log\det\left(\boldsymbol{I}_U + \frac{\alpha_{n,m}^{\mathrm{SD}}\boldsymbol{\Sigma}_{\mathrm{SD}}[n,m]\,\boldsymbol{\Lambda}_{\mathrm{SD}}[n,m]}{N_0}\right) \tag{10}$$

$$R_{\mathrm{DL}}[n] = \sum_{u=1}^{U}\sum_{m\in\mathcal{M}} R_{\mathrm{DL}}^u[n,m] \tag{11}$$

with $R_{\mathrm{DL}}^u[n,m] = (N_s-2)/N_s\log(1+\alpha_{n,m}^{\mathrm{DL}}\mathrm{SINR}_{\mathrm{DL}}^u[n,m])$ and

$\mathrm{SINR}_{\mathrm{DL}}^u[n,m]$

$$\boldsymbol{y}_{\mathrm{SD}}[n,t,m] = \begin{cases}\boldsymbol{0}, & t=1\\ \alpha_{n,m}^{\mathrm{SD}}\widetilde{\boldsymbol{W}}_{\mathrm{SD}}^H[n,m]\,\boldsymbol{H}_{\mathrm{SD}}^H[n,m]\,\boldsymbol{F}_{\mathrm{SD}}[n,m]\,\boldsymbol{x}_{\mathrm{SD}}[n,t,m] & \\ \quad +\widetilde{\boldsymbol{W}}_{\mathrm{SD}}^H[n,m]\,\boldsymbol{n}_{\mathrm{UAV}}[n,m], & t\geq 2\end{cases} \tag{7}$$

$$\boldsymbol{H}_{\mathrm{SD}}[n,m] = \sqrt{\frac{G_{\mathrm{TBS}}^{\mathrm{tx}}G_{\mathrm{UAV}}^{\mathrm{rx}}\lambda_m^2}{(4\pi)^2\,d_{\mathrm{TU}}^2[n]}}e^{-\mathrm{j}2\pi\tau f_m}e^{\mathrm{j}2\pi f_D t_0} \times\left(\sqrt{\frac{K_{\mathrm{TU}}}{K_{\mathrm{TU}}+1}}\varpi_{n,m}\boldsymbol{\alpha}_{\mathrm{tx}}^{\mathrm{TBS}}\left(\theta^{\mathrm{tx}}[n],\phi^{\mathrm{tx}}[n],m\right)\boldsymbol{\alpha}_{\mathrm{rx}}^H\left(\theta^{\mathrm{rx}}[n],\phi^{\mathrm{rx}}[n],m\right)+\sqrt{\frac{1}{K_{\mathrm{TU}}+1}}\boldsymbol{\Psi}_{\mathrm{SD}}[n,m]\right) \tag{8}$$

$$\boldsymbol{y}_{\mathrm{PE}}[n,t,m,m'] = \begin{cases}\boldsymbol{0}, & 1\leq t\leq 3\\ \alpha_{n,m}^{\mathrm{PE}}\widetilde{\boldsymbol{F}}_{\mathrm{PE}}^H[n,m]\,\boldsymbol{H}_{\mathrm{PE}}^H[n,m]\,\boldsymbol{W}_{\mathrm{PE}}[n,m]\,\boldsymbol{r}_{\mathrm{PE}}[n,t,m']+\widetilde{\boldsymbol{F}}_{\mathrm{PE}}^H[n,m]\,\boldsymbol{n}_{\mathrm{TBS}}[n,m], & t\geq 4\end{cases} \tag{9}$$

$$= \frac{p^u_{\mathrm{DL}}[n,m]\,\Omega^u_{\mathrm{DL}}[n,m]}{\sum_{u'=1,u'\neq u}^{U} p^{u'}_{\mathrm{DL}}[n,m]\,\Omega^u_{\mathrm{DL}}[n,m]\left|G^{u',u}_{\mathrm{DL}}[n,m]\right|^2 + N_0} \quad (12)$$

in which $\Omega^u_{\mathrm{DL}}[n,m] = (G^{\mathrm{tx}}_{\mathrm{UAV}} G^{\mathrm{rx}}_{\mathrm{UE}} \lambda_m^2 |\varpi_{u,m}|^2)/((4\pi)^2 d_u^2[n])$ and $G^{u',u}_{\mathrm{DL}}[n,m] = \boldsymbol{\alpha}^H_{\mathrm{tx}}(\theta^{\mathrm{tx}}_u[n], \phi^{\mathrm{tx}}_u[n], m)\boldsymbol{\alpha}_{\mathrm{tx}}(\theta^{\mathrm{tx}}_{u'}[n], \phi^{\mathrm{tx}}_{u'}[n], m)$.

To evaluate the sensing performance, we adopt the MI as a sensing metric,[3] which exhibits the information-theoretic limit on how much environmental information can be exploited, and hence is widely used in the ISAC literature [31], [32]. As seen in (3) and (9), the objective of sensing is to obtain the information of targets included in $\boldsymbol{H}_{\mathrm{SEN}}[n,m']$ based on the perceived signal $\boldsymbol{y}_{\mathrm{PE}}[n,t,m,m']$ at the TBS. Therefore, the end-to-end sensing MI at the nth radio frame is given in (13), as shown at the bottom of the page,

where the entries of $\boldsymbol{G}[n,m']$ are given by $(\boldsymbol{G}[n,m'])_{a,b} = \boldsymbol{\alpha}^H_{\mathrm{rx}}(\theta^{\mathrm{rx}}_a[n], \phi^{\mathrm{rx}}_a[n], m')\boldsymbol{\alpha}_{\mathrm{rx}}(\theta^{\mathrm{rx}}_b[n], \phi^{\mathrm{rx}}_b[n], m')$, $\forall a,b \in \mathcal{J}$, and $\boldsymbol{\Omega}_{\mathrm{SEN}}[n,m']$ is a diagonal matrix with the diagonal entries $(\boldsymbol{\Omega}_{\mathrm{SEN}}[n,m'])_a = (G^{\mathrm{tx}}_{\mathrm{UAV}} G^{\mathrm{rx}}_{\mathrm{UAV}} \lambda^2_{m'} \sigma^{\mathrm{RCS}}_j |\varpi_{j,m'}|^2)/((4\pi)^3 d_j^4[n])$, $\forall a \in \mathcal{J}$, and

$$\begin{aligned}\boldsymbol{\Gamma}\left[n,m,m'\right] = {} & \boldsymbol{\Lambda}^{1/2}_{\mathrm{PE}}[n,m]\,\boldsymbol{\Sigma}^{1/2}_{\mathrm{PE}}[n,m]\,\widetilde{\boldsymbol{W}}^H_{\mathrm{SEN}}\left[n,m'\right] \\ & \times \left(\left(\xi_{\mathrm{SIC}} \times \mathrm{Tr}\left(\boldsymbol{\Sigma}_{\mathrm{SEN}}\left[n,m'\right]\right) + N_0\right)\boldsymbol{I}_{R_{\mathrm{rx}}}\right) \\ & \times \widetilde{\boldsymbol{W}}_{\mathrm{SEN}}\left[n,m'\right]\boldsymbol{\Sigma}^{1/2}_{\mathrm{PE}}[n,m] \\ & \times \boldsymbol{\Lambda}^{1/2}_{\mathrm{PE}}[n,m] + N_0\boldsymbol{I}_J. \end{aligned} \quad (14)$$

According to (10) and (13), the optimization problem can be formulated as

$$(\mathrm{P1}): \quad \max_{\left\{\alpha^X_{n,m},\mathcal{M}^{\mathrm{pair}}_n\right\},\{\boldsymbol{\Sigma}[n,m]\},\{\boldsymbol{c}_{\mathrm{UAV}}[n]\}} \quad \min\left\{R_{\mathrm{SD}}[n], R_{\mathrm{DL}}[n]\right\} \quad (15a)$$

$$\text{s.t. } \alpha^{\mathrm{DL}}_{n,m} + \alpha^{\mathrm{SEN}}_{n,m} + \alpha^{\mathrm{PE}}_{n,m} + \alpha^{\mathrm{SD}}_{n,m} \leq 1 \quad \forall n\ \forall m \in \mathcal{M} \quad (15b)$$

$$\alpha^X_{n,m} \in \{0,1\} \quad \forall n\ \forall m \in \mathcal{M}\ \forall X \quad (15c)$$

$$\sum_{m\in\mathcal{M}} \alpha^{\mathrm{SEN}}_{n,m} = \sum_{m\in\mathcal{M}_n} \alpha^{\mathrm{PE}}_{n,m} = \frac{M}{4} \quad \forall n \quad (15d)$$

$$\sum_{m\in\mathcal{M}} \alpha^{\mathrm{SD}}_{n,m} + \sum_{m\in\mathcal{M}} \alpha^{\mathrm{DL}}_{n,m} = \frac{M}{2} \quad \forall n \quad (15e)$$

$$\sum_{m\in\mathcal{M}} R^u_{\mathrm{DL}}[n,m] \geq R^{\min}_{\mathrm{DL}} \quad \forall n\ \forall u \in \mathcal{U} \quad (15f)$$

$$\sum_{(m,m')\in\mathcal{M}^{\mathrm{pair}}_n} R^j_{\mathrm{MI}}\left[n,m,m'\right] \geq R^{\min}_{\mathrm{MI}} \quad \forall n\ \forall j \in \mathcal{J} \quad (15g)$$

$$\sum_{m\in\mathcal{M}} \alpha^{\mathrm{DL}}_{n,m}\mathrm{Tr}\left(\boldsymbol{\Sigma}_{\mathrm{DL}}[n,m]\right) + \sum_{(m,m')\in\mathcal{M}^{\mathrm{pair}}_n} \times \left(\alpha^{\mathrm{SEN}}_{n,m'}\mathrm{Tr}\left(\boldsymbol{\Sigma}_{\mathrm{SEN}}\left[n,m'\right]\right) + \alpha^{\mathrm{PE}}_{n,m}\alpha^{\mathrm{SEN}}_{n,m'} \times \mathrm{Tr}\left(\boldsymbol{\Pi}_{\mathrm{SEN}}\left[n,m'\right]\boldsymbol{\Sigma}_{\mathrm{PE}}[n,m]\right)\right) \leq P_{\mathrm{UAV}} \quad \forall n \quad (15h)$$

$$\sum_{m\in\mathcal{M}} \alpha^{\mathrm{SD}}_{n,m}\mathrm{Tr}\left(\boldsymbol{\Sigma}_{\mathrm{SD}}[n,m]\right) \leq P_{\mathrm{TBS}} \quad \forall n \quad (15i)$$

$$\left\|\boldsymbol{c}_{\mathrm{UAV}}[n] - \boldsymbol{c}_{\mathrm{UAV}}[n-1]\right\| \leq \frac{T}{N_t}V_{\max} \quad \forall n > 1 \quad (15j)$$

where $\boldsymbol{\Pi}_{\mathrm{SEN}}[n,m'] = \boldsymbol{G}^H[n,m']\boldsymbol{\Omega}_{\mathrm{SEN}}[n,m']\boldsymbol{\Sigma}_{\mathrm{SEN}}[n,m']\boldsymbol{G}[n,m'] + \widetilde{\boldsymbol{W}}^H_{\mathrm{SEN}}[n,m']((\xi_{\mathrm{SIC}}\mathrm{Tr}(\boldsymbol{\Sigma}_{\mathrm{SEN}}[n,m']) + N_0)\boldsymbol{I}_{R_{\mathrm{rx}}})\widetilde{\boldsymbol{W}}_{\mathrm{SEN}}[n,m']$.

The objective function implies that the final end-to-end DL rate is the minimum of the access rate and fronthaul rate. Constraints (15b)–(15e) denote the orthogonality and relative sizes among different subcarrier sets. The user's minimum achievable DL rate requirement at each radio frame is given by (15f). The constraint on the required target estimation accuracy in terms of sensing MI per radio frame is given by (15g), where $R^{\min}_{\mathrm{MI}}$ is the minimum threshold reflecting the basic target characteristics [31]. The maximum transmission power of the UAV and TBS are constrained by (15h) and (15i), respectively. As the velocity of the UAV is lower than $V_{\max}$, the maximum flight distance between two consecutive time slots is constrained in (15j).

Remark 3: Different from terrestrial scenarios where an on-demand UAV is usually deployed nearby and can carry out transmissions immediately after taking off, the departure point of the UAV in the considered maritime scenario is far away from the destination. Due to the extremely high path loss caused by long distance, the performance of DL communication and especially, sensing hardly satisfies the QoS constraints given in (15f) and (15g). Therefore, before handling the optimization problem (P1), it is necessary to first find the initial operating position at which the UAV can simultaneously activate the CAS services toward the emergency area. When the UAV arrives at this initial operating position, it can start to work on solving the optimization problem (P1).

IV. Solutions to Two Subproblems

As discussed in Remark 3, dealing with the problem (P1) amounts to solving the two subproblems consequently.

1) Finding a suitable initial operating position $\boldsymbol{c}_{\mathrm{UAV}}[1]$ at the first radio frame.

[3]Note that there are multiple targets needed to be sensed on the sea surface, and the sensing task for different targets may be distinct. Hence, using MI as the sensing metric makes the formulation of the overall optimization more generic.

$$\begin{aligned} R_{\mathrm{MI}}\left[n,m,m'\right] &= \frac{N_s-3}{N_s}\mathcal{I}\left(\boldsymbol{y}_{\mathrm{PE}}\left[n,t,m,m'\right];\boldsymbol{H}_{\mathrm{SEN}}\left[n,m'\right]\left|\boldsymbol{x}_{\mathrm{SEN}}\left[n,t,m'\right]\right.\right) \\ &= \frac{N_s-3}{N_s}\log\det\Big(\boldsymbol{I}_J + \alpha^{\mathrm{SEN}}_{m',n}\alpha^{\mathrm{PE}}_{n,m}\boldsymbol{\Gamma}^{-1}\left[n,m,m'\right]\boldsymbol{\Lambda}^{1/2}_{\mathrm{PE}}[n,m]\,\boldsymbol{\Sigma}^{1/2}_{\mathrm{PE}}[n,m]\,\boldsymbol{G}\left[n,m'\right]\boldsymbol{\Omega}_{\mathrm{SEN}}\left[n,m'\right] \\ &\qquad \times \boldsymbol{\Sigma}_{\mathrm{SEN}}\left[n,m'\right]\boldsymbol{G}\left[n,m'\right]\boldsymbol{\Sigma}^{1/2}_{\mathrm{PE}}[n,m]\,\boldsymbol{\Lambda}^{1/2}_{\mathrm{PE}}[n,m]\Big) \end{aligned} \quad (13)$$

2) Starting from this initial operating position, optimizing the trajectory and resource allocation to maximize DL rate while guaranteeing sensing QoS.

A. First Subproblem: Finding Initial Operating Position

We assume that the UAV takes off from the coastal base with the coordinate of $\boldsymbol{c}_{\mathrm{UAV}}[0]$. For the purpose of emergency rescue, the UAV is expected to provide prompt CAS services after receiving the command from the TBS. To this end, the distance between $\boldsymbol{c}_{\mathrm{UAV}}[0]$ and $\boldsymbol{c}_{\mathrm{UAV}}[1]$ should be as close as possible, but at the same time, the minimum QoSs of both CAS must be satisfied at $\boldsymbol{c}_{\mathrm{UAV}}[1]$. Hence, the first subproblem can be formulated as follows:

$$(\mathrm{P2}): \min_{\boldsymbol{c}_{\mathrm{UAV}}[1]} \|\boldsymbol{c}_{\mathrm{UAV}}[1]-\boldsymbol{c}_{\mathrm{UAV}}[0]\|^2 \tag{16a}$$

$$\text{s.t. } R_{\mathrm{SD}}[1] \geq UR_{\mathrm{DL}}^{\min} \tag{16b}$$

$$(15\mathrm{b})\text{-}(15\mathrm{i}) \text{ for } n=1. \tag{16c}$$

Constraint (16b) ensures that the fronthaul link is able to support the basic DL communication QoS. The optimization (P2) is challenging to solve directly owing to the nonconvex constraints (15f)–(15h) and the binary integer constraints (15b)–(15e).

1) Transform Subcarrier-Related Constraints: Recall that there are $M/4$ pairs of $(m,m') \in \mathcal{M}_n^{\mathrm{pair}}$ with $m \in \mathcal{M}_n^{\mathrm{PE}}$ and $m' \in \mathcal{M}_n^{\mathrm{SEN}}$, where m' and m are used by the UAV to transmit probing signals and convey the collected sensing data to the TBS, respectively. As the performance loss of UAV–target link is much larger than that of UAV–TBS link, to find a suitable initial position, intuitively, UAV–target links should have the priority to select subcarriers from $\mathcal{M}^S$ such that the sensing QoS can be efficiently satisfied. Hence, for the first radio frame $n=1$, $\alpha_{1,m'}^{\mathrm{SEN}}$ can be determined as follows.[4]

1) Set $\alpha_{1,m'}^{\mathrm{SEN}}=0$, $\forall m' \in \mathcal{M}^S$ and $k=1$.
2) Find m_k' by solving $m_k' = \arg\max_{m' \in \mathcal{M}^S} \mathrm{Tr}(\boldsymbol{\Omega}_{\mathrm{SEN}}[1,m'])$, and update $\alpha_{1,m_k'}^{\mathrm{SEN}}=1$, $\mathcal{M}_1^{\mathrm{SEN}} = \mathcal{M}_1^{\mathrm{SEN}} \cup \{m_k'\}$, and $k=k+1$.
3) Repeat step 2) until $|\mathcal{M}_1^{\mathrm{SEN}}| = M/4$.

Then, we have $\alpha_{1,m}^{\mathrm{PE}}=1$, $m \in \mathcal{M}_1^{\mathrm{PE}}$, where $\mathcal{M}_1^{\mathrm{PE}} = \mathcal{M}^S - \mathcal{M}_1^{\mathrm{SEN}}$. To maximize the end-to-end sensing MI under the greedy principle, $\mathcal{M}_1^{\mathrm{pair}}$ can be determined as follows.

1) Set $\mathcal{M}_1^{\mathrm{pair}}=\emptyset$ and $k=1$.
2) Find m_k by solving $m_k = \arg\max_{m \in \mathcal{M}_1^{\mathrm{PE}}} \mathrm{Tr}(\boldsymbol{\Lambda}_{\mathrm{PE}}[1,m])$, and update $\mathcal{M}_1^{\mathrm{pair}} = \mathcal{M}_1^{\mathrm{pair}} \cup \{(m_k, m_k')\}$ and $k=k+1$.
3) Repeat step 2) until $k=M/4$. So far, $\{\alpha_{1,m}^{\mathrm{PE}}, \alpha_{1,m}^{\mathrm{SEN}}, \mathcal{M}_1^{\mathrm{pair}}\}$ have been determined.

Then, (15b) is reformed as

$$\alpha_{1,m}^{\mathrm{DL}} + \alpha_{1,m}^{\mathrm{SD}} \leq 1 \quad \forall m \in \mathcal{M}^D. \tag{17}$$

The residual binary variables $\alpha_{1,m}^{\mathrm{DL}}$ and $\alpha_{1,m}^{\mathrm{SD}}$ are coupled with $\boldsymbol{\Sigma}_{\mathrm{DL}}[1,m]$ and $\boldsymbol{\Sigma}_{\mathrm{SD}}[1,m]$, respectively, as shown in (15f), (15h), (15i), and (16b), which makes these constraints nonconvex. Basically, there are four possible combinations between the values of DL-related subcarrier indicators and power matrices, which are $\left\{\left(\alpha_{1,m}, \boldsymbol{\Sigma}[1,m]\right) | \alpha_{1,m} \in \{0,1\}, \boldsymbol{\Sigma}[1,m] \in \left\{\mathbf{0}, \bar{\boldsymbol{A}}[1,m]\right\}\right\}$, where $\bar{\boldsymbol{A}}[1,m] \succeq \mathbf{0}$ and $\bar{\boldsymbol{A}}[1,m] \neq \mathbf{0}$. However, it can be seen that only $(0,\mathbf{0})$ and $(1,\bar{\boldsymbol{A}}[1,m])$ can be the feasible solutions for the problem (P2). Take $\alpha_{1,m}^{\mathrm{DL}}$ and $\boldsymbol{\Sigma}_{\mathrm{DL}}[1,m]$ as example. If $(\alpha_{1,m}^{\mathrm{DL}}, \boldsymbol{\Sigma}_{\mathrm{DL}}[1,m]) = (0, \bar{\boldsymbol{A}}[1,m])$, the power allocated to the mth subcarrier have no impact on $R_{\mathrm{DL}}[1]$, and this power will be allocated to other subcarriers to maximize $R_{\mathrm{DL}}[1]$, leading to $\bar{\boldsymbol{A}}[1,m]=\mathbf{0}$ at the end of optimization. If $(\alpha_{1,m}^{\mathrm{DL}}, \boldsymbol{\Sigma}_{\mathrm{DL}}[1,m]) = (1,\mathbf{0})$, the mth subcarrier is wasted as no power is allocated to it. Hence, the optimization is prone to assign subcarrier m to the fronthaul link for transmitting source data from TBS to UAV, as the end-to-end DL rate is the minimum of access and fronthaul rates. Thus, we can remove the binary variables by introducing the auxiliary matrices

$$\begin{aligned}\bar{\boldsymbol{\Sigma}}_{\mathrm{DL}}[1,m] &= \mathrm{diag}\left(\bar{p}_{\mathrm{DL}}^1[1,m], \ldots, \bar{p}_{\mathrm{DL}}^U[1,m]\right) \\ &= \alpha_{1,m}^{\mathrm{DL}} \boldsymbol{\Sigma}_{\mathrm{DL}}[1,m] \\ \bar{\boldsymbol{\Sigma}}_{\mathrm{SD}}[1,m] &= \mathrm{diag}\left(\bar{p}_{\mathrm{SD}}^1[1,m], \ldots, \bar{p}_{\mathrm{SD}}^U[1,m]\right) \\ &= \alpha_{1,m}^{\mathrm{SD}} \boldsymbol{\Sigma}_{\mathrm{SD}}[1,m]. \end{aligned} \tag{18}$$

Then, (17) is converted into

$$\left\|\mathrm{Tr}\left(\bar{\boldsymbol{\Sigma}}_{\mathrm{DL}}[1,m]\right)\right\|_0 + \left\|\mathrm{Tr}\left(\bar{\boldsymbol{\Sigma}}_{\mathrm{SD}}[1,m]\right)\right\|_0 \leq 1 \quad \forall m \in \mathcal{M}^D. \tag{19}$$

A smooth function is adopted to approximate the two nonconvex $\mathcal{L}_0$-norm functions in (19), which is given in (20), as shown at the bottom of the next page, where $X \in \{\mathrm{DL}, \mathrm{SD}\}$. The process of (a) is due to the fact that, $\Upsilon(\bar{\boldsymbol{\Sigma}}_X[1,m])$ is a nondecreasing concave function, and hence, its upper bound at $\bar{\boldsymbol{\Sigma}}_X^{(k)}[1,m]$ can be derived as $\widetilde{\Upsilon}(\bar{\boldsymbol{\Sigma}}_X[1,m])$. In addition, $\rho^{(k)}$ is an iterative smoothing parameter, whose value determines how $\widetilde{\Upsilon}(\bar{\boldsymbol{\Sigma}}_X[1,m])$ behave closer to $\|\mathrm{Tr}(\bar{\boldsymbol{\Sigma}}_X[1,m])\|_0$. If $\rho^{(k)}$ is set too small at the beginning, the optimization process is prone to getting stuck in local optima. Therefore, during the optimization, $\rho^{(k)}$ is first initialized to a larger value, and then gradually decreased as the iteration increases [33].

2) Transform Communication-Related Constraints: Based on (18), $R_{\mathrm{DL}}[1]$ and $R_{\mathrm{SD}}[1]$ are reformulated as

$$\begin{cases} R_{\mathrm{DL}}[1] = \sum_{u=1}^{U} \underbrace{\frac{N_s-2}{N_s} \sum_{m \in \mathcal{M}^D} \log\left(1+\frac{S_{\mathrm{DL}}^u[1,m]}{N_{\mathrm{DL}}^u[1,m]}\right)}_{R_{\mathrm{DL}}^u[1]} \\ R_{\mathrm{SD}}[1] = \sum_{u=1}^{U} \frac{N_s-1}{N_s} \sum_{m \in \mathcal{M}^D} \log\left(1+\frac{S_{\mathrm{SD}}^u[1,m]}{N_{\mathrm{SD}}^u[1,m]}\right) \end{cases} \tag{21}$$

where $S_{\mathrm{DL}}^u[1,m] = \bar{p}_{\mathrm{DL}}^u[1,m]\bar{\Omega}_{\mathrm{DL}}^u[1,m]|G_{\mathrm{DL}}^{u,u}[1,m]|^2$, $S_{\mathrm{SD}}^u[1,m] = \eta_{\mathrm{SD}}^u[1,m]p_{\mathrm{SD}}^u[1,m]$, $N_{\mathrm{DL}}^u[1,m] = \sum_{u'=1,u'\neq u}^{U} \bar{p}_{\mathrm{DL}}^{u'}[1,m]\bar{\Omega}_{\mathrm{DL}}^u[1,m]\left|G_{\mathrm{DL}}^{u',u}[1,m]\right|^2 + N_0 Z_u[1]$, and $N_{\mathrm{SD}}^u[1,m] = N_0 Z_{\mathrm{TU}}[1]$ with $Z_u[1] = d_u^2[1] = (x_{\mathrm{UAV}}[1]-x_u)^2 + (y_{\mathrm{UAV}}[1]-y_u)^2 + (z_{\mathrm{UAV}}-z_u)^2$, $Z_{\mathrm{TU}}[1] = d_{\mathrm{TU}}^2 = (x_{\mathrm{UAV}}[1]-x_{\mathrm{TBS}})^2 + (y_{\mathrm{UAV}}[1]-y_{\mathrm{TBS}})^2 + (z_{\mathrm{UAV}}-z_{\mathrm{TBS}})^2$, and $\Omega_{\mathrm{DL}}^u[1,m] = \bar{\Omega}_{\mathrm{DL}}^u[1,m]/d_u^2[1]$. It can be seen that in (21), $R_{\mathrm{DL}}^u[1]$ is a sum-of-functions-of-ratio

[4] Although the proposed method is suboptimal in terms of performance, its low complexity is more practical for the UAV scenario. Our future work will study the deep reinforcement learning-assisted subcarrier allocation among fronthaul and access links to take both performance and complexity into account.

problem and $S^u_{\mathrm{DL}}[1,m]/N^u_{\mathrm{DL}}[1,m]$ satisfies the form of concave/convex. Hence, we can convexify constraint (15f) in an iterative manner with the aid of quadratic transform [34], which can be expressed as

$$\frac{N_s-2}{N_s}\sum_{m\in\mathcal{M}^D}\log\left(1+2v^{u(k)}_{\mathrm{DL}}[1,m]\sqrt{S^{u(k+1)}_{\mathrm{DL}}[1,m]}-\left(v^{u(k)}_{\mathrm{DL}}[1,m]\right)^2 N^{u(k+1)}_{\mathrm{DL}}[1,m]\right)\triangleq\widetilde{R}^u_{\mathrm{DL}}[1]\geq R^{\min}_{\mathrm{DL}} \tag{22}$$

with $v^{u(k)}_{\mathrm{DL}}[1,m]=(S^{u(k)}_{\mathrm{DL}}[1,m])^{1/2}/N^{u(k)}_{\mathrm{DL}}[1,m],\forall u$. Obviously, when either $\{v^u_{\mathrm{DL}}[1,m]\}$ or $\{\bar{p}^u_{\mathrm{DL}}[1,m],\boldsymbol{c}_{\mathrm{UAV}}[1]\}$ is fixed, $\widetilde{R}^u_{\mathrm{DL}}[1]$ is concave, and hence (22) is a convex constraint. It is also noteworthy that alternately iterating between $\{v^u_{\mathrm{DL}}[1,m]\}$ and $\{\bar{p}^u_{\mathrm{DL}}[1,m],\boldsymbol{c}_{\mathrm{UAV}}[1]\}$ will cause the value of $\widetilde{R}^u_{\mathrm{DL}}[1]$ to increase continuously. Therefore, after several iterations, there will always be a feasible region of $\{\bar{p}^u_{\mathrm{DL}}[1,m],\boldsymbol{c}_{\mathrm{UAV}}[1]\}$ that meets $\widetilde{R}^u_{\mathrm{DL}}[1]\geq R^{\min}_{\mathrm{DL}}$. In this regard, constraint (15f) can be iteratively approximated by (22).

Similarly, constraint (16b) can be convexified as

$$UR^{\min}_{\mathrm{DL}}-\tilde{R}_{\mathrm{SD}}[1]\leq 0 \tag{23}$$

where $\widetilde{R}_{\mathrm{SD}}[1]\triangleq\sum_{m\in\mathcal{M}^D}\sum_{u=1}^{U}(N_s-1)/N_s\log(1+2v^{u(k)}_{\mathrm{SD}}[1,m](S^{u(k+1)}_{\mathrm{SD}}[1,m])^{1/2}-(v^{u(k)}_{\mathrm{SD}}[1,m])^2N^{u(k+1)}_{\mathrm{SD}}[1,m])$ with $v^{u(k)}_{\mathrm{SD}}[1,m]=(S^{u(k)}_{\mathrm{SD}}[1,m])^{1/2}/N^{u(k)}_{\mathrm{SD}}[1,m],\forall u$.

3) Transform Sensing-Related Constraints: In order to transform the MI-related constraints (15g) and (15h) into convex ones, we first present the MI of jth target over (m,m') pair, which is given by

$$R^j_{\mathrm{MI}}\left[1,m,m'\right]=\frac{N_s-3}{N_s}\left(\log\left(S^j_{\mathrm{MI}}\left[1,m,m'\right]\right)-\log\left(N^j_{\mathrm{MI}}\left[1,m,m'\right]\right)\right) \tag{24}$$

where $S^j_{\mathrm{MI}}[1,m,m']$ and $N^j_{\mathrm{MI}}[1,m,m']$ are given in (25) and (26), as shown at the bottom of the page, with the diagonal entry $(\boldsymbol{\Omega}_{\mathrm{SEN}}[1,m'])_{j'}=(\bar{\boldsymbol{\Omega}}_{\mathrm{SEN}}[1,m'])_{j'}/d^4_{j'}[n]$, $Z_{j'}[1]=d^2_{j'}[1]=(x_{\mathrm{UAV}}[1]-x_{j'})^2+(y_{\mathrm{UAV}}[1]-y_{j'})^2+(z_{\mathrm{UAV}}-z_{j'})^2$, and $Z_{\mathrm{TU}}[1]=d^2_{\mathrm{TU}}[1]=(x_{\mathrm{UAV}}[1]-x_{\mathrm{TBS}})^2+(y_{\mathrm{UAV}}[1]-y_{\mathrm{TBS}})^2+(z_{\mathrm{UAV}}-z_{\mathrm{TBS}})^2$. With the aid of the first-order Taylor expansion and successive convex approximation (SCA), $\log(S^j_{\mathrm{MI}}[1,m,m'])$ and $\log(N^j_{\mathrm{MI}}[1,m,m'])$ can be iteratively approximated in a linearized way. The detailed derivation is given in Appendix. Thus, constraint (15g) is reformulated as

$$\sum_{(m,m')\in\mathcal{M}_1^{\mathrm{pair}}}\sum_{j=1}^{J}\left(\widetilde{N}^j_{\mathrm{MI}}\left[1,m,m'\right]-\widetilde{S}^j_{\mathrm{MI}}\left[1,m,m'\right]\right)+\frac{N_sR^{\min}_{\mathrm{MI}}}{N_s-3}\leq 0 \tag{27}$$

which is convex. In addition, the MI-related constraint (15h) can be rewritten as

$$\sum_{m\in\mathcal{M}^D}\mathrm{Tr}\left(\bar{\boldsymbol{\Sigma}}_{\mathrm{DL}}[1,m]\right)+\sum_{(m,m')\in\mathcal{M}_1^{\mathrm{pair}}}\left(\mathrm{Tr}\left(\boldsymbol{\Sigma}_{\mathrm{SEN}}\left[1,m'\right]\right)+\sum_{j=1}^{J}\widetilde{P}^j_{\mathrm{MI}}\left[1,m,m'\right]\right)-P_{\mathrm{UAV}}\leq 0 \tag{28}$$

where $\widetilde{P}^j_{\mathrm{MI}}[1,m,m']$ is the linear approximation of $P^j_{\mathrm{MI}}[1,m,m']$, which is given by

$$P^j_{\mathrm{MI}}\left[1,m,m'\right]=p^j_{\mathrm{PE}}[1,m]\times\left(\sum_{j'=1}^{J}p^{j'}_{\mathrm{SEN}}\left[1,m'\right]\times\left(\left|\left(\boldsymbol{G}\left[1,m'\right]\right)_{j,j'}\right|^2\frac{\left(\bar{\boldsymbol{\Omega}}_{\mathrm{SEN}}[1,m']\right)_{j'}}{Z^2_{j'}[1]}+\xi_{\mathrm{SIC}}\right)+N_0\right). \tag{29}$$

Based on the above transformation, the problem (P2) can be rewritten as

$$(\mathrm{P2.1}):\quad\min_{\boldsymbol{c}_{\mathrm{UAV}}[1]}\|\boldsymbol{c}_{\mathrm{UAV}}[1]-\boldsymbol{c}_{\mathrm{UAV}}[0]\|^2 \tag{30a}$$

$$\text{s.t. }\widetilde{\Upsilon}\left(\bar{\boldsymbol{\Sigma}}_{\mathrm{DL}}[1,m]\right)+\widetilde{\Upsilon}\left(\bar{\boldsymbol{\Sigma}}_{\mathrm{SD}}[1,m]\right)\leq 1\quad\forall m\in\mathcal{M}^D \tag{30b}$$

$$\left\|\mathrm{Tr}\left(\bar{\boldsymbol{\Sigma}}_X[1,m]\right)\right\|_0\approx\Upsilon\left(\bar{\boldsymbol{\Sigma}}_X[1,m]\right)=1-e^{-\frac{\mathrm{Tr}\left(\bar{\boldsymbol{\Sigma}}_X[1,m]\right)}{\rho^{(k)}}}\overset{(a)}{\leq}1-e^{-\frac{\mathrm{Tr}\left(\bar{\boldsymbol{\Sigma}}^{(k)}_X[1,m]\right)}{\rho^{(k)}}}+\frac{1}{\rho^{(k)}}e^{-\frac{\mathrm{Tr}\left(\bar{\boldsymbol{\Sigma}}^{(k)}_X[1,m]\right)}{\rho^{(k)}}}\mathrm{Tr}\left(\bar{\boldsymbol{\Sigma}}_X[1,m]-\bar{\boldsymbol{\Sigma}}^{(k)}_X[1,m]\right)\triangleq\widetilde{\Upsilon}\left(\bar{\boldsymbol{\Sigma}}_X[1,m]\right) \tag{20}$$

$$S^j_{\mathrm{MI}}\left[1,m,m'\right]=\frac{\eta^j_{\mathrm{PE}}[1,m]\,p^j_{\mathrm{PE}}[1,m]}{Z_{\mathrm{TU}}[1]}\left(\sum_{j'=1}^{J}p^{j'}_{\mathrm{SEN}}\left[1,m'\right]\left(\left|\left(\boldsymbol{G}\left[1,m'\right]\right)_{j,j'}\right|^2\frac{\left(\bar{\boldsymbol{\Omega}}_{\mathrm{SEN}}[1,m']\right)_{j'}}{Z^2_{j'}[1]}+\xi_{\mathrm{SIC}}\right)+N_0\right)+N_0 \tag{25}$$

$$N^j_{\mathrm{MI}}\left[1,m,m'\right]=\frac{\eta^j_{\mathrm{PE}}[1,m]\,p^j_{\mathrm{PE}}[1,m]}{Z_{\mathrm{TU}}[1]}\times\left(\sum_{j'=1,j'\neq j}^{J}p^{j'}_{\mathrm{SEN}}\left[1,m'\right]\left|\left(\boldsymbol{G}\left[1,m'\right]\right)_{j,j'}\right|^2\frac{\left(\bar{\boldsymbol{\Omega}}_{\mathrm{SEN}}[1,m']\right)_{j'}}{Z^2_{j'}[1]}+\sum_{j'=1}^{J}p^{j'}_{\mathrm{SEN}}\left[1,m'\right]\xi_{\mathrm{SIC}}+N_0\right)+N_0 \tag{26}$$

$$\sum_{m\in\mathcal{M}^D} \mathrm{Tr}\left(\bar{\boldsymbol{\Sigma}}_{\mathrm{SD}}[1,m]\right) \le P_{\mathrm{TBS}} \tag{30c}$$

$$\left|p_{\mathrm{PE}}^{j(k)}[1,m] - p_{\mathrm{PE}}^{j(k-1)}[1,m]\right| \le \vartheta^{(k)}\mu_p \quad \forall j\in\mathcal{J}\ \forall m\in\mathcal{M}_1^{\mathrm{PE}} \tag{30d}$$

$$\left|p_{\mathrm{SEN}}^{j'(k)}\left[1,m'\right] - p_{\mathrm{SEN}}^{j'(k-1)}\left[1,m'\right]\right| \le \vartheta^{(k)}\mu_s \quad \forall j'\in\mathcal{J}\ \forall m'\in\mathcal{M}_1^{\mathrm{SEN}} \tag{30e}$$

$$\left|x_{\mathrm{UAV}}^{(k)}[1] - x_{\mathrm{UAV}}^{(k-1)}[1]\right| \le \vartheta^{(k)}\mu_x \tag{30f}$$

$$\left|y_{\mathrm{UAV}}^{(k)}[1] - y_{\mathrm{UAV}}^{(k-1)}[1]\right| \le \vartheta^{(k)}\mu_y \tag{30g}$$

$$(22),(23),(27),(28) \tag{30h}$$

where $\vartheta^{(k)}\mu_X$ with $0<\vartheta^{(k)}\le 1$ and $X\in\{p,s,x,y\}$ denotes the specific radius of the trust region. As the linear approximation based on first-order Taylor expansion is used in (27) and (28), we impose constraints (30d)–(30g) to guarantee the accuracy of approximation.

4) Algorithm Implementation: In (P2.1), the involved QoS constraints are carried out in an iterative manner. To implement iterative optimization, it is crucial to find the initial iteration values of power allocation, and the UAV position, i.e., $x_{\mathrm{UAV}}^{(0)}[1]$ and $y_{\mathrm{UAV}}^{(0)}[1]$, within the feasible region, since both CAS performances depend heavily on the lengths of fronthaul and access links. Hence, during the algorithm implementation, we first initialize $\{\bar{p}_{\mathrm{DL}}^{u(0)}[1,m], \bar{p}_{\mathrm{SD}}^{u(0)}[1,m]\}$ and $\{p_{\mathrm{SEN}}^{j'(0)}[1,m']\}$ through equal power allocation. Since $p_{\mathrm{PE}}^{j}[1,m]$ is actually the power coefficient rather than the real power allocated to each target, which is highly related to the UAV position as implied from (29), $\{p_{\mathrm{PE}}^{j(0)}[1,m]\}$ cannot be easily obtained by power equalization. Thus, we derive them by solving the following optimization problem:

(P2.2) :

$$\max_{\left\{p_{\mathrm{PE}}^{j(0)}[1,m]\right\}} \chi \tag{31a}$$

$$\text{s.t.} \sum_{(m,m')\in\mathcal{M}_1^{\mathrm{pair}}} \eta_{\mathrm{PE}}^{j}[1,m]\, P_{\mathrm{MI}}^{j(0)}\left[1,m,m'\right] \ge \chi \quad \forall j\in\mathcal{J} \tag{31b}$$

$$\sum_{m\in\mathcal{M}^D} \mathrm{Tr}\left(\bar{\boldsymbol{\Sigma}}_{\mathrm{DL}}^{(0)}[1,m]\right) + \sum_{(m,m')\in\mathcal{M}_1^{\mathrm{pair}}} \times \left(\mathrm{Tr}\left(\boldsymbol{\Sigma}_{\mathrm{SEN}}^{(0)}\left[1,m'\right]\right) + \sum_{j=1}^{J} P_{\mathrm{MI}}^{j(0)}\left[1,m,m'\right]\right) - P_{\mathrm{UAV}} \le 0 \tag{31c}$$

where constraint (31b) ensures that the initialization of $p_{\mathrm{PE}}^{j(0)}[1,m]$ maximizes the performance of the sensing fronthaul link under fairness consideration.

Moreover, the problem (P2.1) aims to minimize the distance between the initial operating point and the take-off point, and the optimal solution may be several kilometers long, which may cause the problem that the first-order Taylor expansion-based SCA method is susceptible to getting stuck in local optima during the optimization process. In particular, as shown in (30d)–(30g), the size of trust region is limited to μ_X and gradually decreased, such that the nonconvex functions can be well-approximated by linear functions at each iteration point. Hence, when the optimization process of (P2.1) is finished, the local optimal point near the initial iteration point is possibly obtained. To address this issue, we propose an enhanced local approximation (ELA) method using double-layer iteration to handle the optimization. This is to say, at each local optimal point, the searching radius of the trust region is reset to μ_X, thereby forcing the optimization process into a new iteration cycle. This double-layer iteration ends when the global optimal point is found. The detailed implementation of addressing (P2) is summarized in Algorithm 1.

Algorithm 1 Find Initial UAV Operating Position

Initialization:
Give UAV taking off position $\boldsymbol{c}_{\mathrm{UAV}}[0]$ and designated area center $\boldsymbol{c}_{\mathrm{DA}}=(x_{\mathrm{DA}}, y_{\mathrm{DA}}, z_{\mathrm{UAV}})$, set position step size $\boldsymbol{l}_{\mathrm{step}}$, and thresholds ϵ' and ϵ;
Obtain MI-related subcarrier allocation and pairing results $\mathcal{M}_1^{\mathrm{PE}}$, $\mathcal{M}_1^{\mathrm{SE}}$ and $\mathcal{M}_1^{\mathrm{pair}}$;
Set iteration value $k=0$, $d=1$;
Obtain $\bar{p}_{\mathrm{DL}}^{u(k)}[1,m]$, $\bar{p}_{\mathrm{SD}}^{u(k)}[1,m]$, $\forall u\in\mathcal{U}, m\in\mathcal{M}^D$ and $p_{\mathrm{SEN}}^{j'(k)}[1,m']$, $\forall j'\in\mathcal{J}, m'\in\mathcal{M}_1^{\mathrm{SEN}}$ by power equalization;
[Finding initial iteration values of UAV position and power coefficient]
  repeat
    Compute $\boldsymbol{c}_{\mathrm{UAV}}^{(k)}[1]=\boldsymbol{c}_{\mathrm{DA}}-d\cdot\boldsymbol{l}_{\mathrm{step}}$;
    Compute $v_{\mathrm{SD}}^{u(k)}[1,m]=\frac{\sqrt{S_{\mathrm{SD}}^{u(k)}[1,m]}}{N_{\mathrm{SD}}^{u(k)}[1,m]}$, $v_{\mathrm{DL}}^{u(k)}[1,m]=\frac{\sqrt{S_{\mathrm{DL}}^{u(k)}[1,m]}}{N_{\mathrm{DL}}^{u(k)}[1,m]}$, $\forall u\in\mathcal{U}, m\in\mathcal{M}^D$;
    Obtain $p_{\mathrm{PE}}^{j(k)}[1,m], \forall j\in\mathcal{J}, m\in\mathcal{M}_1^{\mathrm{PE}}$ by solving optimization problem (P2.2);
    Leverage all initial iteration values to deal with optimization problem (P2.1);
    if (P2.1) is not solvable **then**
      $d=d+1$;
    end if
  until (P2.1) is solvable;
end
[Applying the ELA method]
  repeat
    Set $k=k+1$, $k'=1$, $\boldsymbol{c}_{\mathrm{UAV}}^{(k')}[1]=\boldsymbol{c}_{\mathrm{UAV}}^{(k-1)}[1]$;
    repeat
      Implement Step 5 and Steps 9-10, and then solve optimization problem (P2.1);
      Set $k'=k'+1$;
      Update $\bar{p}_{\mathrm{DL}}^{u(k')}[1,m]=\bar{p}_{\mathrm{DL}}^{u(k'-1)}[1,m]$, $\bar{p}_{\mathrm{SD}}^{u(k')}[1,m]=\bar{p}_{\mathrm{SD}}^{u(k'-1)}[1,m]$, $\forall m\in\mathcal{M}^D$, and $p_{\mathrm{SEN}}^{j'(k')}[1,m']=p_{\mathrm{SEN}}^{j'(k'-1)}[1,m']$, $p_{\mathrm{PE}}^{j(k')}[1,m]=p_{\mathrm{PE}}^{j(k'-1)}[1,m]$, $\forall(m,m')\in\mathcal{M}_1^{\mathrm{pair}}$, and $\boldsymbol{c}_{\mathrm{UAV}}^{(k')}[1]=\boldsymbol{c}_{\mathrm{UAV}}^{(k'-1)}[1]$;
    until $|\boldsymbol{c}_{\mathrm{UAV}}^{(k')}[1]-\boldsymbol{c}_{\mathrm{UAV}}^{(k'-1)}[1]|\le\epsilon'$;
    Update $\boldsymbol{c}_{\mathrm{UAV}}^{(k-1)}[1]=\boldsymbol{c}_{\mathrm{UAV}}^{(k')}[1]$;
  until $|\boldsymbol{c}_{\mathrm{UAV}}^{(k)}[1]-\boldsymbol{c}_{\mathrm{UAV}}^{(k-1)}[1]|\le\epsilon$;
end
Output : $\boldsymbol{c}_{\mathrm{UAV}}[1]$.

B. Second Subproblem: Optimization From Initial Operating Position Toward Emergency Area

Once the UAV arrives at the initial operating position, it starts to simultaneously carry out CAS tasks with the objective of maximizing the end-to-end DL rate subject to the required

sensing QoS, which leads to the second subproblem expressed as

$$\text{(P3)}:$$

$$\max_{\left\{\alpha_{n,m},\mathcal{M}_n^{\text{pair}}\right\},\{\boldsymbol{\Sigma}[n,m],\boldsymbol{\Sigma}[n,m]\},\{\boldsymbol{c}_{\text{UAV}}[n]\}} \quad \psi \tag{32a}$$

$$\text{s.t. } R_{\text{DL}}[n] \geq \psi \quad \forall n > 1 \tag{32b}$$

$$R_{\text{SD}}[n] \geq \psi \quad \forall n > 1 \tag{32c}$$

$$\sum_{m\in\mathcal{M}^S} \alpha_{n,m}^{\text{SEN}} = \sum_{m\in\mathcal{M}_n^S} \alpha_{n,m}^{\text{PE}} = \frac{M}{4} \quad \forall n > 1 \tag{32d}$$

$$\text{(15j),(27),(28),(30b)-(30g).} \tag{32e}$$

Equations (32b) and (32c) can be convexified by linearizing $R_{\text{DL}}[n]$ and $R_{\text{SD}}[n]$, respectively, following the same method as used in (22) and (23).

Next, we have to deal with constraint (32d), since the MI-related subcarrier allocation in (P3) is totally different from that in (P2). Specifically, after the UAV passes the initial operating position, its relative distances to the TBS and targets are continuously changing, and it is hard to say whether the UAV–target link or UAV–TBS link should have priority in subcarrier allocation. We adopt the following dynamic allocation method for MI-related subcarriers. After the UAV passes the initial operating position, the UAV–target sensing link has the priority to select subcarriers. Following the same method proposed in Section IV-A1, we obtain $\mathcal{M}_2^{\text{PE}}$ and $\mathcal{M}_2^{\text{SEN}}$. After solving (P3), if the sensing performance improves at the second radio frame, i.e., $\sum_{(m,m')\in\mathcal{M}_2^{\text{pair}}} R_{\text{MI}}[2,m,m'] - \sum_{(m,m')\in\mathcal{M}_1^{\text{pair}}} R_{\text{MI}}[1,m,m'] \geq 0$, the same principle is applied at the third radio frame to obtain $\mathcal{M}_3^{\text{PE}}$ and $\mathcal{M}_3^{\text{SEN}}$. Otherwise, at the third radio frame, the two subcarrier sets have to be fine-tuned as follows. First, find $m_i' = \arg\max_{m'\in\mathcal{M}_3^{\text{SEN}}} \text{Tr}(\boldsymbol{\Lambda}_{\text{PE}}[3,m])$ and $m_j = \arg\min_{m\in\mathcal{M}_3^{\text{PE}}} \text{Tr}(\boldsymbol{\Lambda}_{\text{PE}}[3,m])$. Then, implement $\mathcal{M}_3^{\text{SEN}} = (\mathcal{M}_3^{\text{SEN}} - \{m_i'\}) \cup \{m_j\}$ and $\mathcal{M}_3^{\text{PE}} = (\mathcal{M}_3^{\text{PE}} - \{m_j\}) \cup \{m_i'\}$. In addition, the pairing between the subcarriers within $\mathcal{M}_3^{\text{SEN}}$ and $\mathcal{M}_3^{\text{PE}}$ are updated. The process is repeated for $n > 2$ until the end of the mission period.

C. Convergence Analysis and Computational Complexity

1) Convergence Analysis: The convergence of the proposed solutions of the first subproblem [i.e., (P2.1)] and the second subproblem [i.e., (P3)] is mainly based on the trust region-aided SCA methods, the convergence of which has been proved in [35]. In particular, as for the optimization of the first subproblem, after implementing steps 6–15 of Algorithm 1, the feasibly initial iteration value of the UAV position (i.e., $\boldsymbol{c}_{\text{UAV}}^{(0)}[1]$) and its distance with the UAV's take-off point $\mathcal{D}^{(0)} = \|\boldsymbol{c}_{\text{UAV}}^{(0)}[1] - \boldsymbol{c}_{\text{UAV}}[0]\|$ are obtained. Then, within the outer and inner loops of ELA process, as shown in steps 17–27 of Algorithm 1, we have $\mathcal{D}^{(k+1)} \leq \mathcal{D}^{(k)}$ and $\mathcal{D}^{(k'+1)} \leq \mathcal{D}^{(k')}, \forall k$ and k', which shows that the value of the object function of (P2.1) is nonincreasing over iterations. In addition, the distance between $\boldsymbol{c}_{\text{UAV}}[1]$ and $\boldsymbol{c}_{\text{UAV}}[0]$ is lower-bounded due to the constraints of CAS QoSs. As for the optimization of the second subproblem, with the aid of subcarrier iteration and the adjustable radius of trust region $\vartheta^{(k)}$, the objective function of (P3) is nondecreasing over iterations, i.e., $\psi^{(k+1)} \geq \psi^{(k)}$ for each iteration k, and the value of $\psi^{(k)}$ is upper-bounded under the constraints of limited transmit power and flying distance. Therefore, the proposed solutions to the first subproblem and the second subproblem are convergent, which is further numerically demonstrated in Section V-A.

2) Computational Complexity: The computational complexity of solving the first and the second subproblems is attributed to three parts, i.e., 1) the computation of beamforming matrices; 2) MI-related subcarrier allocation and pairing; and 3) the implementation of the involved optimization problems. Since we adopt the low-complexity beamforming design and heuristic method of MI-related subcarrier assignment, the computational complexity of the two subproblems mainly depends on part 3). Then, according to [36], the per-iteration complexity of solving the first and the second subproblems are computed as $\mathcal{O}(((M/2)+(JM)/2+7)^{2.5}((M/2)+(JM)/2+11))$ and $\mathcal{O}(((M/2)+(JM)/2+8)^{2.5}(((UM)/2+(JM)/2+2)^2+(M/2)+(JM)/2+8))$, respectively.

TABLE II
DEFAULT SIMULATION SYSTEM PARAMETERS

Parameters	Values
TBS and UAV power budget ($P_{\text{TBS}}, P_{\text{UAV}}$)	(34, 30) dBm
TBS's transmit and receive antenna gains	(30,26) dBi
UAV's transmit and receive antenna gains	(24,20) dBi
User's receive antenna gain ($G_{\text{UE}}^{\text{rx}}$)	2 dBi
Noise power spectrum density (N_0)	-107 dBm
UAV maximum speed ($V_{\max}$)	30 m/s
Rician factor (K_{TU})	30
RCS ($\sigma_j^{\text{RCS}}, \forall j$)	100 m^2
Central frequency and bandwidth	5 GHz, 10 MHz
Number of subcarriers (M)	32
Azimuth AoD/AoA (ϕ)	$\phi \sim \mathcal{U}(-\pi, \pi)$
Elevation AoD/AoA (θ)	$\theta \sim \mathcal{U}(-\frac{\pi}{2}, \frac{\pi}{2})$
Minimum communication QoS ($R_{\text{DL}}^{\min}$)	10 bit/s/Hz
Minimum sensing QoS ($R_{\text{MI}}^{\min}$)	1 bit/s/Hz

V. SIMULATION AND RESULT ANALYSIS

We consider a coastal emergency scenario centered at $(10^4, 10^4, 0)$ m with a radius of 100 m, where $U = 8$ ships and $J = 4$ potential targets are uniformly distributed. The TBS employs two (8×8) UPAs for transmitting and receiving, respectively, and it is situated at the coordinate of $(0, 0, 10)$ m. The UAV equips two (6×6) UPAs as a transceiver. When receiving the command, it takes off from the coordinate of $(10, 0, 200)$ m and is headed to the emergency area, while its flying height is kept at 200 m. Once arriving at the initial operating position, the UAV commences the CAS works lasting for $T = 500$ s. The number of radio frames within the mission period is $N_t = 500$ and the number of time slots within one radio frame is $N_s = 10$. Other default system parameters are listed in Table II.

A. Convergence Performance of Two Subproblems

Given a random network realization, the convergence behavior of the proposed solutions of the two subproblems is

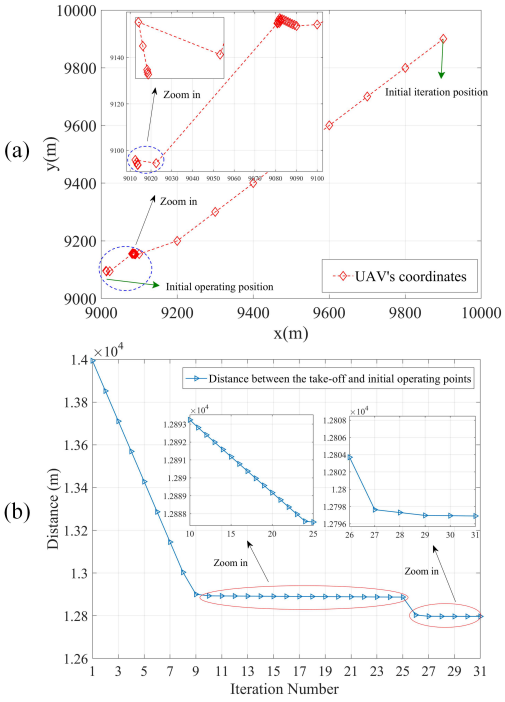

Fig. 3. (a) Update process of the UAV's coordinates and (b) distance change between the UAV's take-off and initial operating points, during the implementation of Algorithm 1, under a random network realization.

depicted as follows. First, as for the first subproblem, Algorithm 1 is applied to find the UAV's initial operating position, and its performance is presented in Fig. 3, where Fig. 3(a) and (b) shows the optimization process of UAV's coordinates and objective value over iterations, respectively. In particular, as shown in Fig. 3(a), based on steps 6–16 of Algorithm 1, the initial iteration value of the UAV position at $(9900, 9900, 200)$ m is determined. Then, by applying the ELA method with a dynamically decreasing factor ϑ, the distance between the UAV's take-off and initial operating points is continuously minimized and converges within 30 iterations. It can be seen from Fig. 3(b) that, compared with iterations 1–10, the object value decreases slowly during iterations 10–30. Accordingly, when considering the system overhead of the UAV, the threshold ϑ can be set to a larger value so as to lower the overall computational complexity.

The optimization process of the second subproblem at one radio frame is plotted in Fig. 4. It can be seen that at the beginning of the iteration process, the access rate is much larger than the fronthaul rate, owing to the fact that the TBS has a higher power budget and the UAV is still far away from the interested area. As the iteration number increases, the UAV moves closer to users and assigns more subcarriers and power to the access links, which enables the end-to-end communication rate to increase until the optimization process converges at the 11th iteration. Although the MI fluctuates during the iteration process, it is restricted in the feasible region such that the sensing performance is guaranteed.

Based on the proposed solutions of two subproblems, the overall optimal UAV trajectory is plotted in Fig. 5, where, for concise presentation, we uniformly sample 20 points starting

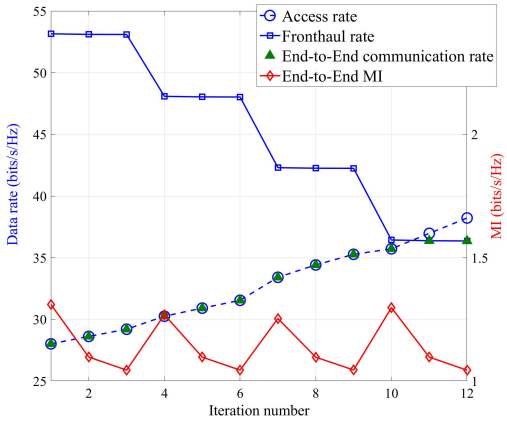

Fig. 4. Convergence behavior of the second subproblem at a random radio frame during mission period.

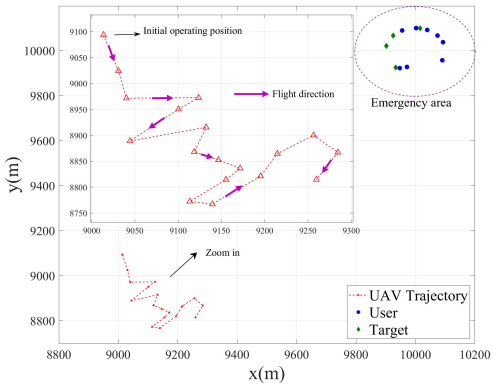

Fig. 5. Overall optimal UAV trajectory under a random network realization.

from the initial operating position during the whole mission period. It can be seen from Fig. 5 that after the initial operating position, the UAV continuously adjusts the direction and the distance among the TBS and emergency area by considering the effects of fronthaul links, to maximize the end-to-end communication rate while maintaining the required sensing performance.

B. Performance of the Proposed Scheme

We further evaluate the performance of the proposed UAV-ISAC MEN. To obtain reliable simulation results, the cumulative distribution function (cdf) performance over thousands of radio frames is evaluated under various network realizations. Fig. 6(a) depicts the network performance under two different sets of UAV and TBS power budgets. When the power budget increases, the TBS and UAV can assign more power to transmit source data and DL data via fronthaul and access links, respectively, which leads to a higher end-to-end communication rate. Specifically, an increase of 4-dBm power at both the UAV and TBS results in an increased 3 bits/s/Hz at a 90% likely rate. By contrast, increasing the power budget imposes a negative effect on the end-to-end MI performance. The reason is that in comparison with sending the sensed

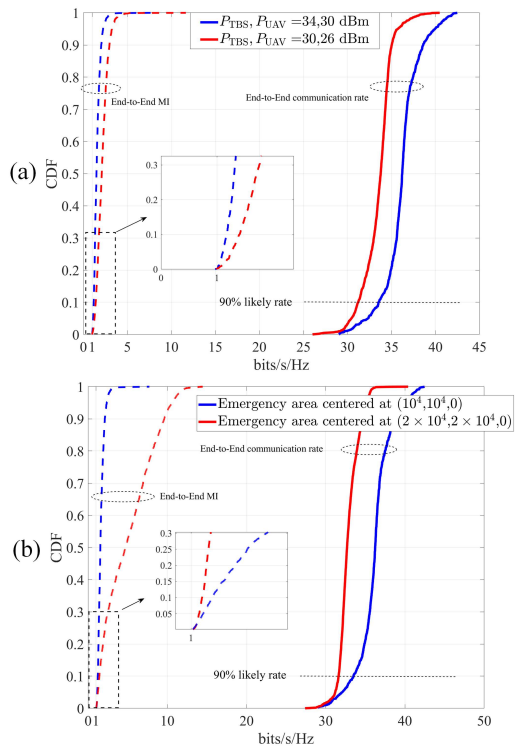

Fig. 6. CDF versus end-to-end communication rate and MI in terms of (a) power budgets and (b) emergency area locations.

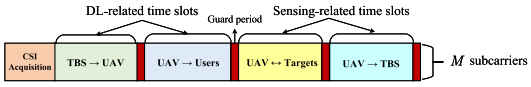

Fig. 7. Radio frame structure of TDD-UAV-ISAC.

information back to the TBS over fronthaul link, the sensing over access links is heavily dependent on the link length, as shown in (13). Therefore, when the power budget is reduced, the UAV is prone to be closer to targets so as to guarantee the required sensing QoS, which leads to an increased end-to-end MI.

Fig. 6(b) studies the impact of emergency area location on the network performance. As expected, the farther the emergency area is situated, the smaller the end-to-end communication rate is. When the emergency area is farther away from the coast, the UAV takes the sensing priority over the access link and therefore tends to fly closer to the targets. To meet the sensing QoS constraint, the UAV may allocate more power to sensing subcarriers, resulting in an increase in the end-to-end MI.

Next, we compare our UAV-ISAC scheme with the following four benchmarks in MENs.

1) *Proposed Scheme With Random Subcarrier Allocation (Proposed Scheme With RanSub):* The subcarrier assignment within $\mathcal{M}^D$ and $\mathcal{M}^S$ is predefined with random selection before the optimization of UAV trajectory and power allocation.
2) *TDD-UAV-ISAC:* The application of TDD in suppressing the interference between CAS links is widely used in UAV-ISAC related works, such as [12], [16], and [25]. To be compatible with the proposed integrated fronthaul-access networks, the radio frame structure of TDD-UAV-ISAC is designed as in Fig. 7. Different from MDD-UAV-ISAC, optimizing the subcarrier allocation, TDD-UAV-ISAC optimizes the time slots assigned to each transmission task, and each transmission task is free to use all the M subcarriers. Note that the guard period is essential to avoid the interference among different transmission tasks, which accounts for one time slot within each radio frame.
3) *Proposed Scheme With Guard Subcarriers (Proposed Scheme With GuaSub):* In practice, to activate the MDD-based scheme, guard subcarriers inserted between different subcarrier blocks are indispensable, so as to avoid the possible intersubcarrier interference caused by imperfect time synchronization. Therefore, to make a fair and reasonable comparison with TDD, the number of guard subcarriers is set to 4, such that the proportion of guard elements is similar to that in TDD.
4) *Straight-Line Flying (S-Line Flying):* Once the UAV arrives at the initial operating position, it flies along the line between the initial operating position and the center of the emergency area. As the trajectory is fixed, the UAV may not meet the sensing or communication QoS requirement at some positions, in which case the UAV is temporarily out of service.
5) *No Sensing-QoS (No Sens-QoS) Constraint:* The UAV carries out DL communication immediately after taking off from the position $(10, 0, 200)$ m, and the sensing QoS constraint is neglected during flying.

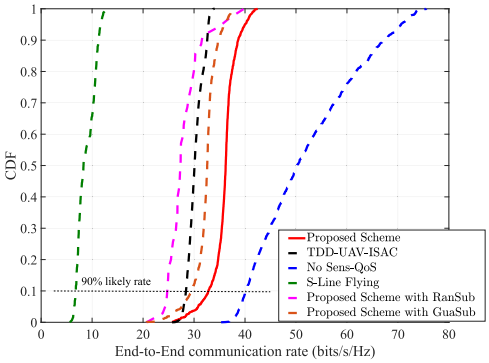

Fig. 8. Network performance comparison for different schemes.

The performance comparison is presented in Fig. 8. No Sens-QoS scheme achieves the highest end-to-end communication rate, but it may not meet the sensing requirement, since the UAV leverages all the resources to implement DL-related transmission over fronthaul and access links. Our proposed UAV-ISAC achieves 5 bits/s/Hz more than the TDD-UAV-ISAC scheme at a 90% likely rate, and this performance advantage is primarily attributed to the fact that there is no resource element to serve as guard intervals. Moreover, even if the proposed scheme applies guard subcarriers for practical concerns, it still outperforms TDD-UAV-ISAC due to the tailor-made FD-like frame structure with four parallel data streams as well as the flexibility in subcarrier allocation.

In addition, the effectiveness of the resource allocation optimization in the proposed scheme is evident as it significantly outperforms Proposed Scheme with RanSub. Without optimizing the UAV's trajectory, the S-Line Flying Scheme attains the lowest end-to-end communication rate.

VI. Conclusion

This article has investigated the UAV-enabled ISAC technique in MENs. Considering that the real-time DL communications and target sensing require the support of robust wireless fronthaul, we have proposed an MDD-based joint

$$\log\left(S_{\mathrm{MI}}^{j}\right) \approx \log\left(S_{\mathrm{MI}}^{j}\right)\Big|_{\mathcal{Q}_{\mathrm{MI}}^{(k)}} + \frac{1}{\ln^2 S_{\mathrm{MI}}^{j}\Big|_{\mathcal{Q}_{\mathrm{MI}}^{(k)}}}\left(\frac{\partial S_{\mathrm{MI}}^{j}}{\partial p_{P}^{j}}\Big|_{\mathcal{Q}_{\mathrm{MI}}^{(k)}}\left(p_{\mathrm{P}}^{j}-p_{\mathrm{P}}^{j(k)}\right)+\sum_{j'}\frac{\partial S_{\mathrm{MI}}^{j}}{\partial p_{\mathrm{S}}^{j'}}\Big|_{\mathcal{Q}_{\mathrm{MI}}^{(k)}}\left(p_{\mathrm{S}}^{j'}-p_{\mathrm{S}}^{j'(k)}\right)\right.$$
$$\left.+\frac{\partial S_{\mathrm{MI}}^{j}}{\partial x_{\mathrm{U}}}\Big|_{\mathcal{Q}_{\mathrm{MI}}^{(k)}}\left(x_{\mathrm{U}}-x_{\mathrm{U}}^{(k)}\right)+\frac{\partial S_{\mathrm{MI}}^{j}}{\partial y_{\mathrm{U}}}\Big|_{\mathcal{Q}_{\mathrm{MI}}^{(k)}}\left(y_{\mathrm{U}}-y_{\mathrm{U}}^{(k)}\right)\right)\triangleq\widetilde{S}_{\mathrm{MI}}^{j} \tag{33}$$

$$\frac{\partial S_{\mathrm{MI}}^{j}}{\partial p_{\mathrm{P}}^{j}}=\sum_{j'=1}^{J}\frac{\eta_{\mathrm{P}}^{j}p_{\mathrm{S}}^{j'}\left|(\boldsymbol{G})_{j,j'}\right|^2(\boldsymbol{\Omega}_{\mathrm{S}})_{j'}}{Z_{\mathrm{TU}}Z_{j'}^2}+\sum_{j'=1}^{J}\frac{\eta_{\mathrm{P}}^{j}p_{\mathrm{S}}^{j'}\xi_{\mathrm{SIC}}}{Z_{\mathrm{TU}}}+\frac{\eta_{\mathrm{P}}^{j}N_0}{Z_{\mathrm{TU}}},\quad \frac{\partial S_{\mathrm{MI}}^{j}}{\partial p_{\mathrm{S}}^{j'}}=\frac{\eta_{\mathrm{P}}^{j}p_{\mathrm{P}}^{j}\left|(\boldsymbol{G})_{j,j'}\right|^2(\boldsymbol{\Omega}_{\mathrm{S}})_{j'}}{Z_{\mathrm{TU}}Z_{j'}^2}+\frac{\eta_{\mathrm{P}}^{j}p_{\mathrm{P}}^{j}\xi_{\mathrm{SIC}}}{Z_{\mathrm{TU}}}$$
$$\frac{\partial S_{\mathrm{MI}}^{j}}{\partial x_{\mathrm{U}}}=\sum_{j'=1}^{J}-\frac{\eta_{\mathrm{P}}^{j}p_{\mathrm{P}}^{j}p_{\mathrm{S}}^{j'}\left|(\boldsymbol{G})_{j,j'}\right|^2(\boldsymbol{\Omega}_{\mathrm{S}})_{j'}}{Z_{\mathrm{TU}}Z_{j'}^2}\left(\frac{4\left(x_{\mathrm{U}}-x_{j'}\right)}{Z_{j'}}+\frac{2\left(x_{\mathrm{U}}-x_{\mathrm{T}}\right)}{Z_{\mathrm{TU}}}\right)-\sum_{j'=1}^{J}\frac{2\eta_{\mathrm{P}}^{j}p_{\mathrm{P}}^{j}p_{\mathrm{S}}^{j'}\xi_{\mathrm{SIC}}\left(x_{\mathrm{U}}-x_{\mathrm{T}}\right)}{Z_{\mathrm{TU}}^2}$$
$$-\frac{\eta_{\mathrm{P}}^{j}p_{\mathrm{P}}^{j}N_0\left(x_{\mathrm{U}}-x_{\mathrm{T}}\right)}{Z_{\mathrm{TU}}^2}$$
$$\frac{\partial S_{\mathrm{MI}}^{j}}{\partial y_{\mathrm{U}}}=\sum_{j'=1}^{J}-\frac{\eta_{\mathrm{P}}^{j}p_{\mathrm{P}}^{j}p_{\mathrm{S}}^{j'}\left|(\boldsymbol{G})_{j,j'}\right|^2(\boldsymbol{\Omega}_{\mathrm{S}})_{j'}}{Z_{\mathrm{TU}}Z_{j'}^2}\left(\frac{4\left(y_{\mathrm{U}}-y_{j'}\right)}{Z_{j'}}+\frac{2\left(y_{\mathrm{U}}-y_{\mathrm{T}}\right)}{Z_{\mathrm{TU}}}\right)-\sum_{j'=1}^{J}\frac{2\eta_{\mathrm{P}}^{j}p_{\mathrm{P}}^{j}p_{\mathrm{S}}^{j'}\xi_{\mathrm{SIC}}\left(y_{\mathrm{U}}-y_{\mathrm{T}}\right)}{Z_{\mathrm{TU}}^2}$$
$$-\frac{\eta_{\mathrm{P}}^{j}p_{\mathrm{P}}^{j}N_0\left(y_{\mathrm{U}}-y_{\mathrm{T}}\right)}{Z_{\mathrm{TU}}^2} \tag{34}$$

$$\log\left(N_{\mathrm{MI}}^{j}\right)\approx\log\left(N_{\mathrm{MI}}^{j}\right)\Big|_{\mathcal{Q}_{\mathrm{MI}}^{(k)}}+\frac{1}{\ln^2 S_{\mathrm{NI}}^{j}\Big|_{\mathcal{Q}_{\mathrm{MI}}^{(k)}}}\left(\frac{\partial N_{\mathrm{MI}}^{j}}{\partial p_{\mathrm{P}}^{j}}\Big|_{\mathcal{Q}_{\mathrm{MI}}^{(k)}}\left(p_{\mathrm{P}}^{j}-p_{\mathrm{P}}^{j(k)}\right)+\sum_{j'}\frac{\partial N_{\mathrm{MI}}^{j}}{\partial p_{\mathrm{S}}^{j'}}\Big|_{\mathcal{Q}_{\mathrm{MI}}^{(k)}}\left(p_{\mathrm{S}}^{j'}-p_{\mathrm{S}}^{j'(k)}\right)\right.$$
$$\left.+\frac{\partial N_{\mathrm{MI}}^{j}}{\partial x_{\mathrm{U}}}\Big|_{\mathcal{Q}_{\mathrm{MI}}^{(k)}}\left(x_{\mathrm{U}}-x_{\mathrm{U}}^{(k)}\right)+\frac{\partial N_{\mathrm{MI}}^{j}}{\partial y_{\mathrm{U}}}\Big|_{\mathcal{Q}_{\mathrm{MI}}^{(k)}}\left(y_{\mathrm{U}}-y_{\mathrm{U}}^{(k)}\right)\right)\triangleq\widetilde{N}_{\mathrm{MI}}^{j} \tag{35}$$

$$\frac{\partial N_{\mathrm{MI}}^{j}}{\partial p_{\mathrm{P}}^{j}}=\sum_{j'=1,j'\neq j}^{J}\frac{\eta_{\mathrm{P}}^{j}p_{\mathrm{S}}^{j'}\left|(\boldsymbol{G})_{j,j'}\right|^2(\boldsymbol{\Omega}_{\mathrm{S}})_{j'}}{Z_{\mathrm{TU}}Z_{j'}^2}+\sum_{j'=1}^{J}\frac{\eta_{\mathrm{P}}^{j}p_{\mathrm{S}}^{j'}\xi_{\mathrm{SIC}}}{Z_{\mathrm{TU}}}+\frac{\eta_{\mathrm{P}}^{j}N_0}{Z_{\mathrm{TU}}}$$
$$\frac{\partial \boldsymbol{N}_{\mathrm{MI}}^{j}}{\partial p_{\mathrm{S}}^{j'}}=\begin{cases}\dfrac{\eta_{\mathrm{P}}^{j}p_{\mathrm{P}}^{j}\left|(\boldsymbol{G})_{j,j'}\right|^2(\boldsymbol{\Omega}_{\mathrm{S}})_{j'}}{Z_{\mathrm{TU}}Z_{j'}^2}+\dfrac{\eta_{\mathrm{P}}^{j}p_{\mathrm{P}}^{j}\xi_{\mathrm{SIC}}}{Z_{\mathrm{TU}}}, & j'\neq j\\ \dfrac{\eta_{\mathrm{P}}^{j}p_{\mathrm{P}}^{j}\xi_{\mathrm{SIC}}}{Z_{\mathrm{TU}}}, & j'=j\end{cases}$$
$$\frac{\partial N_{\mathrm{MI}}^{j}}{\partial x_{\mathrm{U}}}=\sum_{j'=1,j'\neq j}^{J}-\frac{\eta_{\mathrm{P}}^{j}p_{\mathrm{P}}^{j}p_{\mathrm{S}}^{j'}\left|(\boldsymbol{G})_{j,j'}\right|^2(\boldsymbol{\Omega}_{\mathrm{S}})_{j'}}{Z_{\mathrm{TU}}Z_{j'}^2}\left(\frac{4\left(x_{\mathrm{U}}-x_{j'}\right)}{Z_{j'}}+\frac{2\left(x_{\mathrm{U}}-x_{\mathrm{T}}\right)}{Z_{\mathrm{TU}}}\right)$$
$$-\sum_{j'=1}^{J}\frac{2\eta_{\mathrm{P}}^{j}p_{\mathrm{P}}^{j}p_{\mathrm{S}}^{j'}\xi_{\mathrm{SIC}}\left(x_{\mathrm{U}}-x_{\mathrm{T}}\right)}{Z_{\mathrm{TU}}^2}-\frac{\eta_{\mathrm{P}}^{j}p_{\mathrm{P}}^{j}N_0\left(x_{\mathrm{U}}-x_{\mathrm{T}}\right)}{Z_{\mathrm{TU}}^2}$$
$$\frac{\partial N_{\mathrm{MI}}^{j}}{\partial y_{\mathrm{U}}}=\sum_{j'=1,j'\neq j}^{J}-\frac{\eta_{\mathrm{P}}^{j}p_{\mathrm{P}}^{j}p_{\mathrm{S}}^{j'}\left|(\boldsymbol{G})_{j,j'}\right|^2(\boldsymbol{\Omega}_{\mathrm{S}})_{j'}}{Z_{\mathrm{TU}}Z_{j'}^2}\left(\frac{4\left(y_{\mathrm{U}}-y_{j'}\right)}{Z_{j'}}+\frac{2\left(y_{\mathrm{U}}-y_{\mathrm{T}}\right)}{Z_{\mathrm{TU}}}\right)$$
$$-\sum_{j'=1}^{J}\frac{2\eta_{\mathrm{P}}^{j}p_{\mathrm{P}}^{j}p_{\mathrm{S}}^{j'}\xi_{\mathrm{SIC}}\left(y_{\mathrm{U}}-y_{\mathrm{T}}\right)}{Z_{\mathrm{TU}}^2}-\frac{\eta_{\mathrm{P}}^{j}p_{\mathrm{P}}^{j}N_0\left(y_{\mathrm{U}}-y_{\mathrm{T}}\right)}{Z_{\mathrm{TU}}^2} \tag{36}$$

fronthaul-access scheme, where the TBS and UAV exchange the source data and perceived information via fronthaul link, and the UAV transmits ISAC signals via access links. To maximize the end-to-end data rate while guaranteeing the required sensing QoS, we have designed an optimization problem to jointly optimize UAV trajectory, subcarrier, and power allocation, which is divided into two stages for a practical solution, i.e., finding the UAV's initial operating position and optimizing the trajectory and resource allocation in the mission period. The SCA and ELA methods have been applied to address the challenging optimization problem. Numerical results have validated that our proposed scheme is capable of balancing the performance between fronthaul and access links such that the CAS services can be properly carried out during UAV's mission. The advantages of our proposed UAV-ISAC scheme over benchmark schemes have also been demonstrated.

In future work, we will investigate the effects of complex sea conditions (i.e., sea wind and sea clutter) on our proposed UAV-ISAC scheme, and study the strategy of UAV trajectory under sea wind influence as well as sea clutter suppression algorithms to enhance system robustness.

APPENDIX
LINEAR APPROXIMATION OF MI-RELATED FORMULATION

For concise expression, the indices of radio frames and subcarriers are temporarily removed, and notations of PE, SEN, UAV, and TBS are simplified as P, S, U, and T, respectively. Applying SCA, $\log(S^j_{\mathrm{MI}})$ in (24) can be approximated as (33), as shown at the bottom of the previous page, where $\mathcal{Q}^{(k)}_{\mathrm{MI}} = (p^{j(k)}_{\mathrm{P}}, p^{j'(k)}_{\mathrm{S}}, x^{(k)}_{\mathrm{U}}, y^{(k)}_{\mathrm{U}})$, while $(\partial S^j_{\mathrm{MI}})/(\partial p^j_{\mathrm{P}})$, $(\partial S^j_{\mathrm{MI}})/(\partial p^j_{\mathrm{S}})$, $(\partial S^j_{\mathrm{MI}})/(\partial x_{\mathrm{U}})$, and $(\partial S^j_{\mathrm{MI}})/(\partial y_{\mathrm{U}})$ are given in (34), as shown at the bottom of the previous page. Similarly, $\log(N^j_{\mathrm{NI}})$ in (24) can be approximated as (35), as shown at the bottom of the previous page, where $\mathcal{Q}^{(k)}_{\mathrm{MI}'} = (p^{j(k)}_{\mathrm{P}}, p^{j'(k)}_{\mathrm{S}}, x^{(k)}_{\mathrm{U}}, y^{(k)}_{\mathrm{U}})$, while $(\partial N^j_{\mathrm{MI}})/(\partial p^j_{\mathrm{P}})$, $(\partial N^j_{\mathrm{MI}})/(\partial p^{j'}_{\mathrm{S}})$, $(\partial N^j_{\mathrm{MI}})/(\partial x_{\mathrm{U}})$, and $(\partial N^j_{\mathrm{MI}})/(\partial y_{\mathrm{U}})$ are given in (36), as shown at the bottom of the previous page.

REFERENCES

[1] F. S. Alqurashi, A. Trichili, N. Saeed, B. S. Ooi, and M.-S. Alouini, "Maritime communications: A survey on enabling technologies, opportunities, and challenges," *IEEE Internet Things J.*, vol. 10, no. 4, pp. 3525–3547, Feb. 2023.

[2] M. Ilcev, "New aspects for modernization global maritime distress and safety system (GMDSS)," *TransNav, Int. J. Mar. Navigat. Saf. Sea Transp.*, vol. 14, no. 4, pp. 991–998, Mar. 2020.

[3] N. Zhao et al., "UAV-assisted emergency networks in disasters," *IEEE Wireless Commun.*, vol. 26, no. 1, pp. 45–51, Feb. 2019.

[4] X. Gu and G. Zhang, "A survey on UAV-assisted wireless communications: Recent advances and future trends," *Comput. Commun.*, vol. 208, pp. 44–78, Aug. 2023.

[5] M. Kato, T. K. Rodrigues, T. Abe, and T. Suganuma, "Exploiting radio frequency characteristics with a support unmanned aerial vehicle to improve wireless sensor location estimation accuracy," *IEEE Internet Things J.*, vol. 11, no. 24, pp. 39570–39578, Dec. 2024.

[6] K. Meng et al., "UAV-enabled integrated sensing and communication: Opportunities and challenges," *IEEE Wireless Commun.*, vol. 31, no. 2, pp. 97–104, Apr. 2024.

[7] N. Nomikos, P. K. Gkonis, P. S. Bithas, and P. Trakadas, "A survey on UAV-aided maritime communications: Deployment considerations, applications, and future challenges," *IEEE Open J. Commun. Soc.*, vol. 4, pp. 56–78, 2023.

[8] L. Lyu, Z. Chu, B. Lin, Y. Dai, and N. Cheng, "Fast trajectory planning for UAV-enabled maritime IoT systems: A fermat-point based approach," *IEEE Wireless Commun. Lett.*, vol. 11, no. 2, pp. 328–332, Feb. 2022.

[9] L. P. Qian, H. Zhang, Q. Wang, Y. Wu, and B. Lin, "Joint multi-domain resource allocation and trajectory optimization in UAV-assisted maritime IoT networks," *IEEE Internet Things J.*, vol. 10, no. 1, pp. 539–552, Jan. 2023.

[10] Y. Xin, W. Zhao, L. Ma, Y. Ning, P. Shi, and T. Liu, "Joint processing of pilot and data in UAV-aided maritime communications," in *Proc. IEEE/CIC Int. Conf. Commun. China*, Aug. 2023, pp. 1–6.

[11] D. Zhai, Y. Jiang, Q. Shi, R. Zhang, H. Cao, and F. R. Yu, "Joint resource management and deployment optimization for heterogeneous aerial networks with backhaul constraints," *IEEE Trans. Commun.*, vol. 72, no. 1, pp. 348–360, Jan. 2024.

[12] D. Liu, Y. Gao, S. Hu, W. Ni, and X. Wang, "Trajectory design for integrated sensing and communication enabled by cellular-connected UAV," *IEEE Wireless Commun. Lett.*, vol. 13, no. 7, pp. 1973–1977, Jul. 2024.

[13] X. Wang, Z. Fei, J. A. Zhang, J. Huang, and J. Yuan, "Constrained utility maximization in dual-functional radar-communication multi-UAV networks," *IEEE Trans. Commun.*, vol. 69, no. 4, pp. 2660–2672, Apr. 2021.

[14] K. Meng, Q. Wu, S. Ma, W. Chen, K. Wang, and J. Li, "Throughput maximization for UAV-enabled integrated periodic sensing and communication," *IEEE Trans. Wireless Commun.*, vol. 22, no. 1, pp. 671–687, Jan. 2023.

[15] Z. Lyu, G. Zhu, and J. Xu, "Joint maneuver and beamforming design for UAV-enabled integrated sensing and communication," *IEEE Trans. Wireless Commun.*, vol. 22, no. 4, pp. 2424–2440, Apr. 2023.

[16] X. Liu, Y. Liu, Z. Liu, and T. S. Durrani, "Fair integrated sensing and communication for multi-UAV-enabled Internet of Things: Joint 3-D trajectory and resource optimization," *IEEE Internet Things J.*, vol. 11, no. 18, pp. 29546–29556, Sep. 2024.

[17] C. Deng, X. Fang, and X. Wang, "Beamforming design and trajectory optimization for UAV-empowered adaptable integrated sensing and communication," *IEEE Trans. Wireless Commun.*, vol. 22, no. 11, pp. 8512–8526, Nov. 2023.

[18] A. Khalili, A. Rezaei, D. Xu, F. Dressler, and R. Schober, "Efficient UAV hovering, resource allocation, and trajectory design for ISAC with limited backhaul capacity," *IEEE Trans. Wireless Commun.*, vol. 23, no. 11, pp. 17635–17650, Nov. 2024.

[19] Y. Pan et al., "Cooperative trajectory planning and resource allocation for UAV-enabled integrated sensing and communication systems," *IEEE Trans. Veh. Technol.*, vol. 73, no. 5, pp. 6502–6516, May 2024.

[20] T. Zhang, K. Zhu, S. Zheng, D. Niyato, and N. C. Luong, "Trajectory design and power control for joint radar and communication enabled multi-UAV cooperative detection systems," *IEEE Trans. Commun.*, vol. 71, no. 1, pp. 158–172, Jan. 2023.

[21] Z. Liu, X. Liu, Y. Liu, V. C. M. Leung, and T. S. Durrani, "UAV assisted integrated sensing and communications for Internet of Things: 3D trajectory optimization and resource allocation," *IEEE Trans. Wireless Commun.*, vol. 23, no. 8, pp. 8654–8667, Aug. 2024.

[22] O. Rezaei, M. M. Naghsh, S. M. Karbasi, and M. M. Nayebi, "Resource allocation for UAV-enabled integrated sensing and communication (ISAC) via multi-objective optimization," in *Proc. IEEE Int. Conf. Acoust., Speech Signal Process. (ICASSP)*, Jun. 2023, pp. 1–5.

[23] X. Jing, F. Liu, C. Masouros, and Y. Zeng, "ISAC from the sky: UAV trajectory design for joint communication and target localization," *IEEE Trans. Wireless Commun.*, vol. 23, no. 10, pp. 12857–12872, Oct. 2024.

[24] G. A. Bayessa, R. Chai, C. Liang, D. Kumar Jain, and Q. Chen, "Joint UAV deployment and precoder optimization for multicasting and target sensing in UAV-assisted ISAC networks," *IEEE Internet Things J.*, vol. 11, no. 20, pp. 33392–33405, Oct. 2024.

[25] X. Zheng, Y. Wu, L. Fan, X. Lei, R. Qingyang Hu, and G. K. Karagiannidis, "Dual-functional UAV-empowered space-air-ground networks: Joint communication and sensing," *IEEE J. Sel. Areas Commun.*, vol. 42, no. 12, pp. 3412–3427, Dec. 2024.

[26] B. Li, L.-L. Yang, R. G. Maunder, P. Xiao, and S. Sun, "Multicarrier-division duplex: A duplexing technique for the shift to 6G wireless communications," *IEEE Veh. Technol. Mag.*, vol. 16, no. 4, pp. 57–67, Dec. 2021.

[27] B. Debaillie et al., "Analog/RF solutions enabling compact full-duplex radios," *IEEE J. Sel. Areas Commun.*, vol. 32, no. 9, pp. 1662–1673, Sep. 2014.

[28] E. Everett, A. Sahai, and A. Sabharwal, "Passive self-interference suppression for full-duplex infrastructure nodes," *IEEE Trans. Wireless Commun.*, vol. 13, no. 2, pp. 680–694, Feb. 2014.

[29] K. E. Kolodziej, J. G. McMichael, and B. T. Perry, "Multitap RF canceller for in-band full-duplex wireless communications," *IEEE Trans. Wireless Commun.*, vol. 15, no. 6, pp. 4321–4334, Jun. 2016.

[30] B. Li, L.-L. Yang, R. G. Maunder, and S. Sun, "Self-interference cancellation and channel estimation in multicarrier-division duplex systems with hybrid beamforming," *IEEE Access*, vol. 8, pp. 160653–160669, 2020.

[31] C. Shi, F. Wang, M. Sellathurai, J. Zhou, and S. Salous, "Power minimization-based robust OFDM radar waveform design for radar and communication systems in coexistence," *IEEE Trans. Signal Process.*, vol. 66, no. 5, pp. 1316–1330, Mar. 2018.

[32] C. Ouyang, Y. Liu, H. Yang, and N. Al-Dhahir, "Integrated sensing and communications: A mutual information-based framework," *IEEE Commun. Mag.*, vol. 61, no. 5, pp. 26–32, May 2023.

[33] F. Zhuang and V. K. N. Lau, "Backhaul limited asymmetric cooperation for MIMO cellular networks via semidefinite relaxation," *IEEE Trans. Signal Process.*, vol. 62, no. 3, pp. 684–693, Feb. 2014.

[34] K. Shen and W. Yu, "Fractional programming for communication systems—Part I: Power control and beamforming," *IEEE Trans. Signal Process.*, vol. 66, no. 10, pp. 2616–2630, May 2018.

[35] R. L. Burden et al., *Numerical Analysis*. Boston, MA, USA: Cengage Learning, 2015.

[36] H. V. Nguyen, V.-D. Nguyen, O. A. Dobre, Y. Wu, and O.-S. Shin, "Joint antenna array mode selection and user assignment for full-duplex MU-MISO systems," *IEEE Trans. Wireless Commun.*, vol. 18, no. 6, pp. 2946–2963, Jun. 2019.